STOCHASTIC MODELING OF KARLOTOXIN'S INFLUENCE ON PREY

by

Hansen Pei

A dissertation submitted to the Faculty of the University of Delaware in partial fulfillment of the requirements for the degree of Doctor of Philosophy in Applied Mathematics

Summer 2021

STOCHASTIC MODELING OF KARLOTOXIN'S INFLUENCE ON PREY

by

Hansen Pei

Approved: _____
Mark Gockenbach, Ph.D.
Chair of the Department of Mathematical Science

Approved: _____
John Pelesko, Ph.D.
Dean of the College of Science and Engineering

Approved: _____
Louis F. Rossi, Ph.D.
Vice Provost for Graduate and Professional Education and
Dean of the Graduate College

I certify that I have read this dissertation and that in my opinion it meets the academic and professional standard required by the University as a dissertation for the degree of Doctor of Philosophy.

Signed: _____

Louis F. Rossi, Ph.D.
Professor in charge of dissertation

I certify that I have read this dissertation and that in my opinion it meets the academic and professional standard required by the University as a dissertation for the degree of Doctor of Philosophy.

Signed: _____

Pak-Wing Fok, Ph.D.
Member of dissertation committee

I certify that I have read this dissertation and that in my opinion it meets the academic and professional standard required by the University as a dissertation for the degree of Doctor of Philosophy.

Signed: _____

Tobin Driscoll, Ph.D.
Member of dissertation committee

I certify that I have read this dissertation and that in my opinion it meets the academic and professional standard required by the University as a dissertation for the degree of Doctor of Philosophy.

Signed: _____

Claudio Torres, Ph.D.
Member of dissertation committee

ACKNOWLEDGEMENTS

I am sincerely grateful to my advisors, Dr. Louis Rossi and Dr. Pak-Wing Fok, for them providing great support, ideas and effort in the academic guidance throughout all these years. Their co-advisory has enlightened my learning path to conduct research, to think methodologically, to be creative and to mature as an applied mathematician. Especially during the COVID pandemic when the face-to-face communication is not a choice, they have kept patiently providing great feedback and insights for my research project.

I want to thank my parents for their support and encouragement of my pursuit of the degree in applied mathematics abroad. It would be close to impossible to transfer to the US in the first place during college without their dedicated effort, and it was not an easy or obvious decision back then. Also I want to thank many people inside and outside of the university who have kindly spent time personally aiding me in formulating ideas, going over technical details and seeing possibilities, especially Navid Mirzaei and Jacques Joubert.

I have enjoyed my Ph.D. years at University of Delaware largely because of the great staff and faculties in the department of mathematical science. Apart from my advisors, I want to thank all the professors I have taken classes from, especially Dr. Francisco Sayas, Dr. Rakesh, Dr. David Colton, Dr. David Edward and Dr. Mokshay Madiman. Also I want to thank our previous department secretary Ms. Deborah See, who is one of the most kindhearted person I have met at UD, and has always been radiating a lighthearted atmosphere to her surroundings.

I would also like to thank the Blues/Jazz/Tango dancing communities. Though strictly speaking they are not as mathematical, I have learned the mentality on how to adventure into a completely new field quickly, and also how to train and compete like

an athlete. This exercise has also kept my health in shape, and I have met numerous interesting people from there that I would have otherwise missed.

Last but not least, I would like to thank everyone that has decided to openly share their lectures and other high quality academic resources online for free, especially during the pandemic. I was able to keep learning from various interesting topics post-candidacy, and absorb much invaluable insights that have greatly polished my skills and complemented my graduate school training in various quantitative fields.

TABLE OF CONTENTS

LIST OF TABLES

LIST OF FIGURES

ABSTRACT

Karlodinium veneficium is type of dinoflagellate that feeds on planktonic species such as *Storeatula major*. It is associated with fish kills due to harmful algae blooms by releasing a compound called Karlotoxin. This toxin is known to affect their prey's bio-locomotion by stunning them and slowing them down. In this dissertation, we investigate whether the toxin plays a crucial role in aggregating the prey around the predators. The effect of aggregating prey around the predators is ecologically significant since it greatly boosts *K. veneficium*'s feeding and reproduction rate, leading to a population surge, eluding a possible mechanism for producing algal blooms.

We closely examine the toxin's influence on the prey's probability density distribution under the Goldstein-Kac modeling framework with different assumptions on their relative speed in 1-D, with either the predator being stationary or swimming at a constant speed. When the predator is stationary, we fully solve the prey's density distribution for all times, and verify the result by a Monte-Carlo simulation. For a swimming predator, we find the steady-state density distribution of prey analytically. When the predator's speed is strictly greater (or less) than the prey, the results are verified by Monte-Carlo simulations. When their relative speed has roots, singularities occur in the Goldstein-Kac system, and we perform a local analysis for prey's density at steady-state near the roots using the method of Frobenius, and use the result to derive a scheme for finding the analytical solution. For the relative speed in this case, assuming a right-swimming Karlodinium, the roots will occur at the left and right of the Karlodinium and we can get at worst an integrable singularity and at least a local maximum in the wake (the left root), depending on the flipping rate and the slope of the relative speed at this root. Near the other root, the prey's density in either direction can be represented by a Taylor series and is thus smooth. With the presence

of roots for the relative speed, the analytical solution is verified by a finite difference scheme due to poor performance in Monte-Carlo simulations.

For all the cases mentioned above, toxin changes the prey's distribution and in most cases leads to aggregation, however the maximum density does not always occur where the toxin has the highest concentration. In reality, such a result suggests that toxin density greatly influences the prey's distribution, however the distribution is also a result of predator and prey's relative movement. When their relative speed is of single sign, the toxin dominates. When their relative speed fluctuates around 0, both the toxin and their relative movements contributes to prey's distribution.

Chapter 1

INTRODUCTION

1.1 Motivation

Karlodinium veneficium is a type of phytoplankton present in coastal regions in the ocean. *K. veneficium* are mixotrophic species, capable of photosynthesis and preying on multiple plankton species such as *Storeatula major*. Occasionally large scale algal blooms occur in a coastal environment due to population surge of *K. veneficium*, turning the sea water brown. Such algal blooms occur more frequently when their habitat environment is ideal in terms of temperature, nutrient level, predators etc. However, it is also known that its photosynthesis is not strong enough to support such a macro scale algal bloom. Studies have shown that the consumption of prey contributes largely to their nutrient intake, thereby leading to a population surge (Place et al., 2012; Sheng et al., 2010).

Some strains of *K. veneficium* are capable of releasing a toxin, called Karlotoxin, especially in the presence of prey. The toxin slows down and stuns the prey, potentially providing the predator with an advantage by aiding the feeding process. Also, this toxin pollutes the surrounding water and kills fish during large scale algal blooms, resulting in enormous ecologic and economic impact upon coastal communities (Place et al., 2012; Sheng et al., 2010). While it is intuitive to suppose that slowing down and stunning surrounding prey provide an edge for the predator, the standalone impact of toxin on prey aggregation has yet to be fully explored.

1.2 Literature Review

In a series of studies conducted by Sheng et al, with the aid of digital holographic microscopy devices, the full 3-D swimming trajectories of *K. veneficium* and its prey *S.*

major were captured and analyzed. In its summary statistics, the prey has relatively large acceleration value and small radius in its helical trajectory, alongside with the ability to swim in straight lines in the presence of a predator (Sheng et al., 2010).

Studies that quantitatively examined the legitimacy of the run-and-tumble model for microswimmers focused mostly around *E. coli*, with some of the most influential work done in Berg's seminal book (Berg, 2008), where the run-and-tumble movement is described as moving mostly in a straight line, with intermittent sudden directional changes. The run-and-tumble mechanism specifically is described as the *E. coli* rotating their motors clockwise and counterclockwise to control their flagella. Specifically, when the flagella rotate counterclockwise, they lead to a straight swimming motion; when they rotate clockwise, *E. coli* tumbles instead due to its physical shape. The run-and-tumble behavior leads to those observed zigzagging swimming trajectories (Berg and Brown, 1972; Berg, 2008). Childs and Keener (2018) modeled the exact bio-mechanism of the stochastic direction switching between clockwise and counterclockwise rotation of the motor as a Markov process. They managed to greatly reduce the total states of the motor to 2 under moderate assumptions with good fit to the available switching frequency data. They provided justification for the run-and-tumble model, confirming that such an abstraction is not an over-simplification for micro swimmer movements driven by flagella, which is the case for the prey species such as *S. major* (Cerino and Zingone, 2006).

Swimmers react to their nearby chemical environment. There are two types of reaction mechanisms: chemotaxis where the swimmer reacts to the chemical gradient, and chemokinesis where swimmer reacts to just the chemical density (Hillen and Painter, 2009). For both mechanisms, studies of the swimmers' bio-locomotion have been conducted under different frameworks, and there are two main types of models: The Brownian type that is diffusive in nature with independent Gaussian increments for any time interval (therefore infinite speed in the sense of infinite total variation within any time interval, and infinitely frequent direction changes), which usually leads to parabolic equations; and the jump-process type such that the tumbles

(direction changes) are modeled as a discrete arrival process with the speed of the swimmer being finite in between adjacent direction changes, which often leads to hyperbolic equations derived from the conservation law. There are representative models such as the Keller-Segel model (Keller and Segel, 1970) and the Goldstein-Kac model (Goldstein, 1951; Kac, 1974) respectively for the Brownian and the jump-process type, studying chemotaxis and chemokinesis. Both models aim to capture some key aspects of the observed random walk from microswimmers, with the jump-process model generally considered appropriate at relatively smaller temporal and spatial scales, and the Brownian model suitable for larger scales such as in an ecosystem.

With no further quantitative measurements of *S. major*'s movements available, we decide to adopt the commonly used run-and-tumble model under the Goldstein-Kac framework (Goldstein, 1951; Kac, 1974), as it provides great flexibility for describing the stochastic nature of their movements. Holmes (1993) conducted a direct comparison between the two frameworks and concluded that the difference is only significant under fast reproduction or ecological invasion, whereas under moderate biological circumstances the differences are small. Stevens and Othmer (1997) gave definitions for population aggregation, blow-up and collapse, for small organisms moving under the influence of a modulator substance. They showed that finite-time blowup can happen with superlinear growth of the modulator, and a collapse in population density happens with only linear growth rates. D'Orsogna et al. (2003) compared and disentangled self-generated chemotaxis and chemokinesis, focusing on a single cell, and had results verified by agent-based Monte-Carlo simulations. Hillen (2002) started from the Goldstein-Kac model and derived that under different dimensions and limit conditions, this model can approach a Brownian motion with different diffusivities. Taktikos et al. (2011) conducted a thorough analysis on autochemotaxis, studying microswimmers under signaling particles released by themselves, and concluded that even under strong attractive autochemotaxis the long-time diffusion is still present, and attractive autochemotaxis leads to aggregation. For our analysis, we study the aggregation of prey assuming that the strength of Karlotoxin is fully described by the toxin's concentration,

and the toxin influences the bio-locomotion of prey by slowing them down.

For finding analytical solutions under the Goldstein-Kac framework, Martens et al. (2012) fully solved the 2-D run-and-tumble problem under constant speed and complete randomization of directions after each tumble by comparing it with the Lorentz kinetic model for electrons. Recently Angelani and Garra (2019) specifically studied the 1-D version of run-and-tumble with spatially varying speed, under several boundary conditions in a finite domain.

Aside from achieving analytical solutions, agent-based simulations of microswimmers also pose challenges. With simulation, swimmers can react in a more complicated manner to their environment. Emonet et al. (2005) created the AgentCell platform to simulate cell motions in 3-D, taking account of various biochemical processes within the cell. Lushi and Peskin (2013) took into account hydrodynamic flows generated by swimmers and their effect on aggregation and pattern formation in a confined space, verified by laboratory observations.

However, few authors have studied the density of microswimmers analytically under the assumption of a chemical field with evolving concentrations. The evolving Karlotoxin concentration is suggested by the following key observations: First, toxic compounds diffuse and decay. Second, the source of Karlotoxin, the Karlodinium species, are active chasing predators (Place et al., 2012; Sheng et al., 2010). Third, the near field concentration of toxin around predators is high (Sheng et al., 2010). Therefore we aim to investigate the influence of toxin upon prey under some assumptions of an evolving toxin field that are simplifications of such marine environments. This is a first step toward understanding the more complex dynamic systems that exist in the real world.

In this thesis, we first propose a variant of Goldstein-Kac PDE system for the prey's density to account for the run-and-tumble motions and the speed's dependence upon the toxin concentration. Our results are verified by agent-based Monte-Carlo simulations of the original plankton behavioral model. Then, in the presence of a single swimming *K. veneficium*, we discuss the steady-state distributions for the prey's

density which depends strongly on the prey's speed relative to the predator. When their relative speed has no roots, the global analytical solution is found and verified by Monte-Carlo. When the prey and predator's relative speed has roots, various types of singularities occur in the system that fundamentally change the location of prey's maximum density. In addition, the PDE system fails to be strictly hyperbolic at the roots. We investigate the local behaviors of the solution near the singularities, and then propose a scheme for finding the global analytical solution of swimmer's density and verify it through finite difference. The fact that such richness and complexity entail from such a simple model holds its own charm and may further lead to potential abstract studies in the PDE system itself.

1.3 Goldstein-Kac Model Overview

The Goldstein-Kac model originally arises from studying 1-D random walks in continuous space and time: assuming the random walker can move either to the left or right at a constant speed s, and the time interval length in between two adjacent direction changes is distributed exponentially with rate F. Further, assuming the direction switching is instantaneous, we arrive at the following coupled PDEs:

$$\begin{cases} \frac{\partial P_+}{\partial t}(x,t) + s\frac{\partial P_+}{\partial t}(x,t) = FP_-(x,t) - FP_+(x,t), \\ \frac{\partial P_-}{\partial t}(x,t) - s\frac{\partial P_-}{\partial t}(x,t) = FP_+(x,t) - FP_-(x,t), \end{cases} \tag{1.1}$$

where $P_+(x,t)$ is the probability density for a right-moving random walker at (x,t), and $P_-(x,t)$ is the same but for a left-moving random walker.

This model is a great starting point for analyzing the classic run-and-tumble models in 1-D, and a sizable amount of studies have been conducted on studying its diffusion limits such as by Hillen (2002) and by Holmes (1993). Further generalizations can be taken, for example, by having different flipping rate for left-to-right and right-to-left, or letting random time between two adjacent direction changes following another distribution that is not exponential.

One may also recognize its similarity to 1-D Broadwell equations that are used for modeling gas molecules introduced by Broadwell (1964), except that the source

terms on the right hand side of the equations are from particle collision instead of spontaneous direction switching. Indeed, both the Broadwell model and the Goldstein-Kac model come from the overarching conservation law of the following form:

$$\frac{\partial}{\partial t}\int_{\Omega}\mathbf{u}d\Omega+\int_{\Omega}\nabla\cdot\mathbf{f}(\mathbf{u})d\Omega=\int_{\Omega}\mathbf{g}(\mathbf{u})d\Omega, \tag{1.2}$$

for some quantity $\mathbf{u}$ with flux $\mathbf{f}$ and source function $\mathbf{g}$.

1.4 Dissertation Outline

The work presented in this dissertation is divided into the following chapters.

Chapter 1 gives the biological background of our work, the qualitative description of the problem and the a short introduction to the Goldstein-Kac model. We also review different approaches for related topics, especially random walkers under the influence of chemicals.

Chapter 2 introduces the governing equations we use in our model. At first we derive the Goldstein-Kac PDEs that we will use in 1-D, starting from a generic 2-D conservation law. Also we prove the equivalence of two models based on the Goldstein-Kac PDEs used in Hillen (2002) and Othmer et al. (1988). We then establish the evolution equation for the toxin's concentration, and we non-dimensionalize it and derive its steady-state solution.

Chapter 3 discusses in detail under different situations, how the toxin influences the concentration of the prey density. Specifically we cover the case when the toxin concentration is static, and the steady-state case when the predator (source of the toxin) moves at a constant speed. In some situations singularities occur in the system, making the prey aggregate not around the predator but at the wake. When the predator moves, we also discuss the characteristic curves of the system and how they influence the aggregation. When the relative speed has roots, we present the local analysis near the roots using the method of Frobenius, and then derive the global analytical solution using the result. Overall, we manage to find the analytical solutions for all of the situations.

Chapter 4 examines the numerical methods that are used to validate our analytical solutions. Specifically we incorporate a Monte-Carlo scheme when its applicable. When the predator and prey's relative speed has simple roots, the Monte-Carlo scheme performs poorly, and we use a modified finite difference scheme for our result. We explain in detail of both the Monte-Carlo algorithm and the finite difference scheme of our choice. In the end, we compare and justify the analytical results from Chapter 3 with our numerical solutions.

Chapter 5 arrives at the conclusions for our work, and discusses the biological interpretation of our key results. We also briefly summarizes our major analytical and numerical methods with connections to previous work. We then layout our future work and discuss the potential research directions.

Chapter 2

GOVERNING EQUATIONS

2.1 Derivation of Goldstein-Kac Equations

We first present a model for the prey's probability density P on a 2-D domain, then focus on the 1-D case. We assume that the prey do not interact with each other and they move independently. Since the only role of *K. veneficium* is to release background toxin, we just need to model the density function of the prey in the presence of Karlotoxin. Without ambiguity, we can refer to prey as "swimmers". The concentration of toxin is denoted $c(\mathbf{x}, t)$, and the speed of a swimmer, $s(c)$, depends solely on the spot toxin concentration. The swimmer may run and tumble, and the turning frequency or turning rate is F, a constant. Suppose further that the time taken to change direction is zero (i.e., turning is instantaneous). The velocity of the swimmer is $\mathbf{v}$ satisfying $|\mathbf{v}| = s$ with an associated angle, or "state" $\phi \in [0, 2\pi)$, measured relative to a fixed positive direction. Thus, as discussed by Othmer et al. (1988); Hillen (2002), from conservation of the prey's population we have:

$$\frac{\partial}{\partial t}P(\phi, \mathbf{x}, t) + \nabla \cdot (\mathbf{v}P(\phi, \mathbf{x}, t)) = -FP(\phi, \mathbf{x}, t) + F\int_0^{2\pi} T(\phi, \phi')P(\phi', \mathbf{x}, t)d\phi'. \tag{2.1}$$

The right hand side of (2.1) represents all possible ways that swimmers can leave or enter a state ϕ: The first term represents swimmers tumbling away from the state ϕ with rate F (the flip rate); The second term represents swimmers transitioning from a state ϕ' to the state ϕ, $\phi \neq \phi'$, again with rate F. We have further assumed that when a tumble occurs the speed of the swimmer does not change.

Here, $T(\phi, \phi')$ is the angular probability transition kernel of the direction ϕ in the new state, given the angle ϕ' in the previous state. There are two common approaches

to reduce (2.1) to 1-D introduced by Othmer et al. (1988) and Hillen (2002). We adopt Othmer's form in which the new angle ϕ after a tumble must be different from the old angle ϕ'. In contrast, in Hillen's derivation, $\phi = \phi'$ is allowed for each tumble. We later will prove the two approaches can indeed describe the same stochastic process with appropriate flip rates F respectively in Sec. 2.1.1.

Equation (2.1) has been widely used to describe other similar systems such as bacteria run-and-tumble (Berg, 2008) and gas dynamics (Christlieb et al., 2004). Note that analytical solutions for (2.1) are quite difficult to achieve in general, even under moderately simple assumptions on the transition kernel.

To reduce (2.1) to 1-D, introduce the unit radial vector $\mathbf{e}(\phi) = (\cos(\phi), \sin(\phi))$ for convenience. Specifically, $\mathbf{e}(0) = (1, 0)$ and $\mathbf{e}(\pi) = (-1, 0)$. We can then write

$$\mathbf{v}(\phi, \mathbf{x}, t) = \mathbf{e}(\phi)s(c) = \mathbf{e}(\phi)s(\mathbf{x}, t),$$

where the Karlotoxin concentration $c(\mathbf{x}, t)$ is assumed to only influence the swimming speed, not the angle during a tumble. In 1-D, we have only two directions and we can let $\phi \in \{0, \pi\}$ without loss of generality. We get $v = e(\phi)s(x, t) = \pm s(x, t)$. Assuming equal preference in both swimming directions for all tumbles, we must have in 1-D:

$$T(\phi, \phi') = \delta(\phi' - \phi - \pi),$$

because the only angle that ϕ can come from that is not ϕ must be $\phi + \pi$. Thus (2.1) becomes

$$\frac{\partial}{\partial t}P(\phi, x, t) + \frac{\partial}{\partial x}(e(\phi)s(x, t)P(\phi, x, t)) = -FP(\phi, x, t) + FP(\phi + \pi, x, t), \tag{2.2}$$

where $e(0) = 1$ and $e(\pi) = -1$. It is convenient to denote $P(\phi = 0, x, t) = P_+(x, t)$, the probability density for right-moving swimmers and $P(\phi = \pi, x, t) = P_-(x, t)$ for the left-moving swimmers. We arrive at the following Goldstein-Kac system with generalized flux terms:

$$\begin{cases} \frac{\partial}{\partial t}P_+(x, t) + \frac{\partial}{\partial x}\left[s(x, t)P_+(x, t)\right] = F(P_-(x, t) - P_+(x, t)), \\ \frac{\partial}{\partial t}P_-(x, t) - \frac{\partial}{\partial x}\left[s(x, t)P_-(x, t)\right] = F(P_+(x, t) - P_-(x, t)). \end{cases} \tag{2.3}$$

Indeed, if we further let $s(x,t)$ be a constant, then we reproduce the original Goldstein-Kac equations in (1.1). To distinguish from the non-dimensional terms that will be used for the majority of our analysis later, we rewrite all dimensional terms in 1-D that have dimensionless counterparts with a hat. Therefore (2.3) becomes:

$$\begin{cases} \frac{\partial}{\partial \hat{t}}\hat{P}_+(\hat{x},\hat{t}) + \frac{\partial}{\partial \hat{x}}[\hat{s}(\hat{x},\hat{t})\hat{P}_+(\hat{x},\hat{t})] = F(\hat{P}_-(\hat{x},\hat{t}) - \hat{P}_+(\hat{x},\hat{t})) \\ \frac{\partial}{\partial \hat{t}}\hat{P}_-(\hat{x},\hat{t}) - \frac{\partial}{\partial \hat{x}}[\hat{s}(\hat{x},\hat{t})\hat{P}_-(\hat{x},\hat{t})] = F(\hat{P}_+(\hat{x},\hat{t}) - \hat{P}_-(\hat{x},\hat{t})). \end{cases} \tag{2.4}$$

All the systems discussed in this dissertation are solved assuming periodic boundary conditions. We achieve this by equating each probability current's inflow and outflow at each end of the domain. If the domain has length L,

$$\hat{s}(0,\hat{t})\hat{P}_+(0,\hat{t}) = \hat{s}(L,\hat{t})\hat{P}_+(L,\hat{t}), \tag{2.5}$$

$$\hat{s}(L,\hat{t})\hat{P}_-(L,\hat{t}) = \hat{s}(0,\hat{t})\hat{P}_-(0,\hat{t}). \tag{2.6}$$

2.1.1 The Equivalence of Two Popular Models

Consider a continuous time stochastic process $\{v(t)\}_{t\geq 0}$ with state space $\{-1,1\}$ and time t. With the above setting, Othmer's approach (Othmer et al. 1988) and Hillen's approach (Hillen 2002) can be expressed as the following two models, and we aim to show their equivalence for a given positive constant F.

Model 1 (Othmer): Consider the homogeneous Poisson counting process $N_1(t)$ with event interarrival time $\tau_1 \sim Exp(F)$, $N_1(0) = 0$. N_1 must increase its value by 1 at each event, and $v_1(t) = (-1)^{N_1(t)}$. Here N_1 is the counter for the number of events. Since in this approach every new swimming direction has to come from a previously different direction, N_1 increases at each event, and therefore is the counter for the effective number of direction changes.

Model 2 (Hillen): Consider the homogeneous Poisson counting process $N_2(t)$ with event interarrival time $\tau_2 \sim Exp(2F)$, $N_2(0) = 0$. Suppose another stochastic process $N_2^*(t)$ defined recursively as:

1. $N_2^*(0) = 0$;

2. Suppose t_i $(i \geq 1)$ is the time for the i-th increment in $N_2(t)$, and set $t_0 = 0$ then

$$N_2^*(t) = \begin{cases} N_2^*(t_{i-1}), & t \in (t_{i-1}, t_i), \\ X + N_2^*(t_i^-), & t = t_i, \end{cases}$$

where X is a Bernoulli random variable with state space $\{0, 1\}$, independent from the stochastic processes N_1 and N_2, and takes each value with equal probability.

Then we define $v_2(t) = (-1)^{N_2^*(t)}$. Here N_2 is the counter for the number of events but N_2^* is the counter for the effective number of direction changes. They are not equivalent under Hillen's model because at each tumble, the "new" swimming angle can come from the same angle, where it is not counted towards an effective direction change.

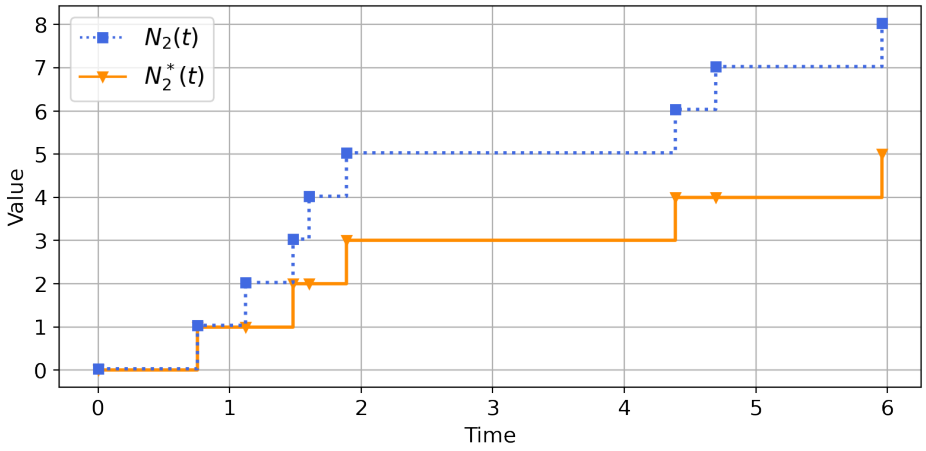

Figure 2.1: A realization of the $N_2(t)$ and an associated $N_2^*(t)$ stochastic process using $F = 1$.

To prove the two models' equivalence, it is sufficient to prove that for all $t \geq 0$:

$$Prob(v_1 = 1, t) = Prob(v_2 = 1, t). \tag{2.7}$$

Proof. For model 1,

$$Prob(v_1 = 1, t) = Prob\{N_1(t) \text{ is even}\} = \sum_{n=0}^{\infty} \frac{(Ft)^{2n} e^{-Ft}}{(2n)!} = e^{-Ft} \cosh(Ft). \tag{2.8}$$

For model 2, the process is equivalent to tossing a fair coin whenever an event occurs for the process N_2: If the result is head then increment N_2^* by 1, if the result is tail then do not increment N_2^*. Using the result below

$$Prob\{\text{number of heads is even in } n \text{ tosses}\} = \frac{1}{2}, \quad n \geq 1, \tag{2.9}$$

we arrive at

$$\begin{aligned} Prob(v_2 = 1, t) &= Prob\{N_2^*(t) \text{ is even}\} \\ &= Prob\{N_2(t) = 0\} \\ &+ \sum_{n=1}^{\infty} Prob\{N_2(t) = n\} Prob\{\text{number of heads is even in } n \text{ tosses}\} \\ &= e^{-2Ft} + \frac{1}{2} \sum_{n=1}^{\infty} \frac{(2Ft)^n e^{-2Ft}}{n!} \\ &= e^{-2Ft} \left(\frac{1}{2} + \frac{1}{2} \sum_{n=0}^{\infty} \frac{(2Ft)^n}{n!} \right) \\ &= e^{-2Ft} \left(\frac{1 + e^{2Ft}}{2} \right) \\ &= e^{-Ft} \cosh(Ft). \end{aligned} \tag{2.10}$$

□

2.2 Evolution of Toxin Concentration

In our model, the speed $|\mathbf{v}|$ depends on the toxin concentration because Karlotoxin has the effect of slowing down the swimmers. We propose the following evolutionary model for the toxin concentration $c(\mathbf{x}, t)$ for a constantly moving toxin source (the predator) to pair with (2.1): Assume the predator is moving with a constant velocity $\mathbf{v_0}$ in an unbounded domain. The predator secretes toxin at a constant rate α. The toxin particle diffuses with rate κ and decays with rate β. This whole process is governed by the following PDE:

$$c_t = \kappa \nabla^2 c - \beta c + \alpha \delta(\mathbf{x} - \mathbf{v_0} t - \gamma), \tag{2.11}$$

where κ, β are positive constants, and γ is the source's starting position. $\delta(\mathbf{x})$ is the multi-dimensional dirac-delta function, representing the point source releasing toxin.

We focus on the steady-state solution in the reference frame of the predator for $P_\pm$ in (2.4) over a periodic domain. In general, the problem for the conservation system in (2.4) with evolving flux terms is quite difficult to solve analytically. For its well-posedness and stability, comprehensive analysis is done in the book by Bastin and Coron (2016). To begin with, we need to find the steady-state solution for the toxin concentration. In 1-D (2.11) becomes:

$$\hat{c}_{\hat{t}} = \hat{\kappa}\hat{c}_{\hat{x}\hat{x}} - \hat{\beta}\hat{c} + \hat{\alpha}\delta(\hat{x} - s_0\hat{t} - \hat{\gamma}). \tag{2.12}$$

Its non-dimensional solution is constructed as follows: Set $\hat{t} = \frac{t}{F}$, $\hat{x} = \frac{s_0 x}{F}$ and $\hat{c} = \frac{\hat{\alpha}c}{s_0}$, where the quantities without the hat accent are dimensionless. We have

$$c_t = \frac{\hat{\kappa}F}{s_0^2}c_{xx} - \frac{\hat{\beta}}{F}c + \delta(x - t - \frac{F\hat{\gamma}}{s_0}). \tag{2.13}$$

Introduce the Galilean transformation $x \leftarrow\!\shortmid x - t$:

$$c_t = \frac{\hat{\kappa}F}{s_0^2}c_{xx} + c_x - \frac{\hat{\beta}}{F}c + \delta(x - \frac{F\hat{\gamma}}{s_0}). \tag{2.14}$$

Then we replace $\frac{\hat{\kappa}F}{s_0^2} = \kappa$, $\frac{\hat{\beta}}{F} = \beta$ and $\frac{F\hat{\gamma}}{s_0} = \gamma$. See Table 2.1 for a summary of definitions. Now drop the temporal term for the steady-state solution:

$$0 = \kappa c'' + c' - \beta c + \delta(x - \gamma). \tag{2.15}$$

This moving reference frame approach is also present in the work by Fu et al. (2018) for analyzing traveling bands of *E. Coli* in a thin channel. We at first solve (2.15) for c_u over an unbounded domain and then derive the periodic domain solution c from it. Eq. 2.15 in an unbounded domain can be solved by Fourier transform:

Suppose we define the Fourier transform and its inverse transform as follows:

$$\mathcal{F}[c_u](\omega) = \frac{1}{\sqrt{2\pi}}\int_{-\infty}^{\infty} c_u(x)e^{i\omega x}dx = \tilde{c}_u(\omega),$$

$$\mathcal{F}^{-1}[\tilde{c}_u](x) = \frac{1}{\sqrt{2\pi}}\int_{-\infty}^{\infty} \tilde{c}_u(\omega)e^{-i\omega x}d\omega = c_u(x).$$

Take the Fourier transform of (2.15) we get

$$\tilde{c}_u(\omega) = \frac{e^{i\gamma\omega}}{\sqrt{2\pi}(\kappa\omega^2 + i\omega + \beta)}.$$

Now we take its inverse Fourier transform and for convenience denote $r_1 = \frac{-1+\sqrt{1+4\beta\kappa}}{2\kappa}$, $r_2 = \frac{-1-\sqrt{1+4\beta\kappa}}{2\kappa}$. Then we have the unbounded domain solution:

$$c_u(x) = \frac{-e^{r_1(x-\gamma)}(1 - H(x-\gamma)) - e^{r_2(x-\gamma)}(1 - H(\gamma - x))}{\sqrt{1+4\beta\kappa}}, \tag{2.16}$$

where H is the Heaviside step function of x, with $H(0) = \frac{1}{2}$.

We then use the unbounded domain solution $c_u(x)$ to construct the solution $c(x)$ corresponding to the periodic boundary condition with non-dimensionalized domain length 1. Indeed, $c_u(x) = c_u(x;\gamma)$ from (2.15) is a Green's function. Periodically extending the source term to $\sum_n \delta(x+n-\gamma)$, we achieve the solution on this periodic domain by periodically summing $c_u(x)$ up:

$$c(x) = \sum_{n=-\infty}^{\infty} c_u(x+n), \quad x \in [0,1]. \tag{2.17}$$

In the absence of more quantitative data, we assume an algebraic dependence of s on c, with $s'(c) < 0$. Note that since c came from (2.17), by definition it is periodic, and thus s should automatically be periodic. It then forces $P_\pm$ to be periodic because of the periodic boundary condition in (2.5) and (2.6).

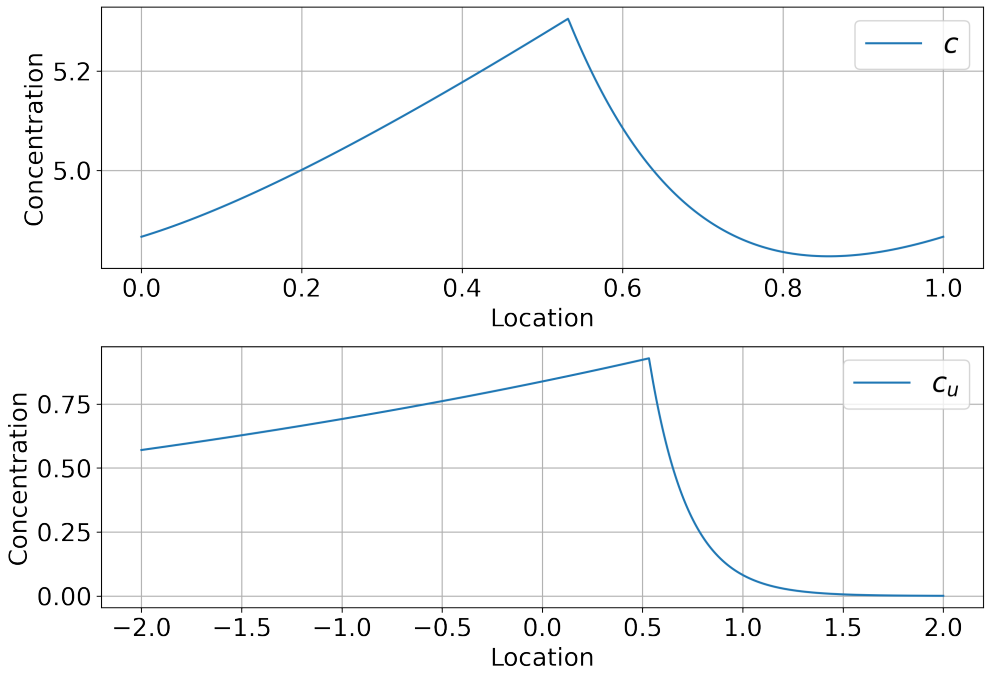

Figure 2.2: Plot of c and c_u. Here $\gamma = 0.532154$, $\beta = 0.2$, $\kappa = 0.2$.

Table 2.1: Dimensionless variables and parameters

Dimensionless Variable or Parameter	Definition	Meaning
x	$\frac{F\hat{x}}{s_0}$	Spatial variable
t	$\hat{t}F$	Temporal variable
β	$\frac{\hat{\beta}}{F}$	Decay constant
κ	$\frac{F\hat{\kappa}}{s_0^2}$	Diffusion constant
γ	$\frac{F\hat{\gamma}}{s_0}$	Initial location of Karlodinium
c	$\frac{s_0\hat{c}}{\hat{\alpha}}$	Karlotoxin concentration
s	$\frac{\hat{s}}{s_0}$	Prey swimming speed
$P_\pm$	$\frac{s_0\hat{P}_\pm(\hat{x},\hat{t})}{F}$	Probability density

Chapter 3

ONE DIMENSIONAL MODEL PROBLEMS

In 1-D, the Goldstein-Kac model allows one to study in general how the swimming speed $\hat{s}(\hat{x}, \hat{t})$ and thus the toxin influences the prey's density distribution. It is the first step to understanding the more general 2-D and 3-D models, and the 1-D structure allows us to do more analysis in depth.

3.1 Modeling Stationary Toxin Concentration

We start our analysis from the generic 1-D model in (2.4) and assume a steady-state distribution of toxin concentration across the domain, i.e., $\hat{c} = \hat{c}(\hat{x})$ and therefore we write $\hat{s}(\hat{c}(\hat{x})) = \hat{s}(\hat{x})$ when no ambiguity arises. Recalling (2.4),

$$\begin{cases} \frac{\partial}{\partial \hat{t}} \hat{P}_+(\hat{x}, \hat{t}) + \frac{\partial}{\partial \hat{x}} [\hat{s}(\hat{x}) \hat{P}_+(\hat{x}, \hat{t})] = F(\hat{P}_-(\hat{x}, \hat{t}) - \hat{P}_+(\hat{x}, \hat{t})) \\ \frac{\partial}{\partial \hat{t}} \hat{P}_-(\hat{x}, \hat{t}) - \frac{\partial}{\partial \hat{x}} [\hat{s}(\hat{x}) \hat{P}_-(\hat{x}, \hat{t})] = F(\hat{P}_+(\hat{x}, \hat{t}) - \hat{P}_-(\hat{x}, \hat{t})) \end{cases} . \tag{3.1}$$

We are in fact studying the more general case for a spatially dependent swimming speed.

We still impose the periodic boundary conditions on the probability current flow as in (2.5, 2.6). Moreover, we impose the following regularity constraints for $\hat{s}(\hat{x})$ to allow further analysis:

(s1) $\hat{s}(\hat{x}) > 0$;

(s2) $\hat{s}(\hat{x})$ is continuous;

(s3) $\hat{s}(\hat{x})$ is analytic in the domain except at finitely many points.

3.1.1 Solution Procedure

We aim to solve the system (3.1) analytically. Decoupling $\hat{P}_+$ and $\hat{P}_-$ in (3.1) leads to the following system:

$$\begin{cases} \frac{\partial^2 \hat{P}_+}{\partial \hat{t}^2} + 2F\frac{\partial \hat{P}_+}{\partial \hat{t}} = \frac{\partial}{\partial \hat{x}}\left[\hat{s}(\hat{x})\frac{\partial}{\partial \hat{x}}\left(\hat{s}(\hat{x})\hat{P}_+\right)\right] \\ \frac{\partial^2 \hat{P}_-}{\partial \hat{t}^2} + 2F\frac{\partial \hat{P}_-}{\partial \hat{t}} = \frac{\partial}{\partial \hat{x}}\left[\hat{s}(\hat{x})\frac{\partial}{\partial \hat{x}}\left(\hat{s}(\hat{x})\hat{P}_-\right)\right] \end{cases}, \tag{3.2}$$

with periodic boundary conditions. The full initial conditions of (3.2) need to be addressed separately as follows: for both equations in (3.1), suppose that we have the initial probability density functions $\hat{P}_\pm(\hat{x},0)$, we also need to find $\frac{\partial}{\partial t}\hat{P}_\pm(\hat{x},0)$. We rearrange (3.1) to obtain

$$\begin{cases} \frac{\partial \hat{P}_+(\hat{x},0)}{\partial \hat{t}} = -\frac{\partial}{\partial \hat{x}}[\hat{s}(\hat{x})\hat{P}_+(\hat{x},0)] + F(\hat{P}_-(\hat{x},0) - \hat{P}_+(\hat{x},0)), \\ \frac{\partial \hat{P}_-(\hat{x},0)}{\partial \hat{t}} = \frac{\partial}{\partial \hat{x}}[\hat{s}(\hat{x})\hat{P}_-(\hat{x},0)] + F(\hat{P}_+(\hat{x},0) - \hat{P}_-(\hat{x},0)). \end{cases} \tag{3.3}$$

Thus $\hat{P}_\pm(\hat{x},0)$ determine $\frac{\partial}{\partial \hat{t}}\hat{P}_\pm(\hat{x},0)$. To solve this problem, we need to further conduct several transformations: First, We define the flux in the positive and negative direction at $(\hat{x},\hat{t})$ respectively as

$$M_\pm(\hat{x},\hat{t}) = \pm\hat{s}(\hat{x})\hat{P}_\pm(\hat{x},\hat{t}). \tag{3.4}$$

Next, define $y(\hat{x})$ by $d\hat{x} = \hat{s}(\hat{x})dy$ with $y(0) = 0$. This implies $\frac{\partial}{\partial y} = \frac{\partial}{\partial \hat{x}}\frac{d\hat{x}}{dy} = \hat{s}(\hat{x})\frac{\partial}{\partial \hat{x}}$ and therefore

$$y(\hat{x}) = \int_0^{\hat{x}} \frac{1}{\hat{s}(z)}dz. \tag{3.5}$$

Hence $y \in [0,l]$, where $l = \int_0^L \frac{1}{\hat{s}(\hat{x})}d\hat{x}$. We effectively defined a bijective mapping between the original spatial domain in $\hat{x}$ and another domain in y measured in time. This domain mapping turns out to be related with the system's characteristic curves. Indeed, $y(\hat{x})$ coincides with the characteristic curve $\hat{t}(\hat{x})$ starting at $\hat{x} = 0$ for P_+. The characteristics will be discussed in detail in Sec. 3.2.1.1 and Sec. 3.2.2.1. We will also revisit this domain mapping idea in Sec. 4.1.2 for conducting the Monte-Carlo simulation.

The physical meaning of the y-coordinate is the time taken for a right-moving swimmer to travel from the origin to $\hat{x}(y)$ with no change in direction. Angelani and

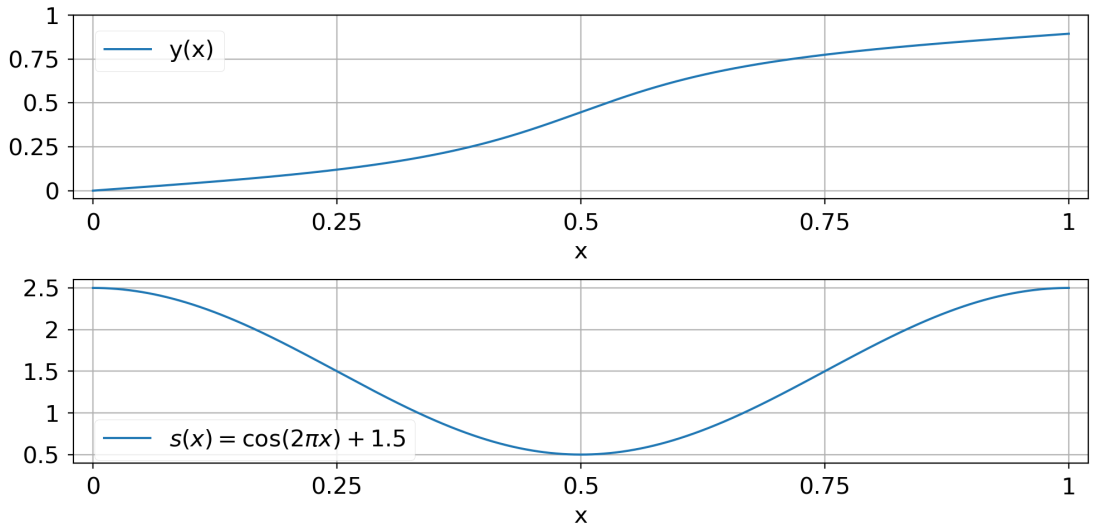

Figure 3.1: Plot of $y(x)$ when $s(x) = \cos(2\pi x) + 1.5$ for $x \in [0, 1]$.

Garra (2019) conducted this transformation for solving (3.2) under other boundary conditions.

From now on, we denote $M_{\pm}(\hat{x}(y), \hat{t})$ as $M_{\pm}(y, \hat{t})$, $\hat{s}(\hat{x}(y))$ as $\hat{s}(y)$, $\hat{P}_{\pm}(\hat{x}(y), 0)$ as $\hat{P}_{\pm}(y, 0)$. Multiplying both equations of (3.2) by $\hat{s}(\hat{x})$,

$$\begin{cases} \frac{\partial^2 \hat{s}(\hat{x})\hat{P}_+}{\partial \hat{t}^2} + 2F\frac{\partial \hat{s}(\hat{x})\hat{P}_+}{\partial \hat{t}} = \hat{s}(\hat{x})\frac{\partial}{\partial \hat{x}}\left[\hat{s}(\hat{x})\frac{\partial}{\partial \hat{x}}\left(\hat{s}(\hat{x})\hat{P}_+\right)\right] \\ \frac{\partial^2 \hat{s}(\hat{x})\hat{P}_-}{\partial \hat{t}^2} + 2F\frac{\partial \hat{s}(\hat{x})\hat{P}_-}{\partial \hat{t}} = \hat{s}(\hat{x})\frac{\partial}{\partial \hat{x}}\left[\hat{s}(\hat{x})\frac{\partial}{\partial \hat{x}}\left(\hat{s}(\hat{x})\hat{P}_-\right)\right] \end{cases}, \tag{3.6}$$

and using

$$\frac{\partial}{\partial y} = \hat{s}(\hat{x})\frac{\partial}{\partial \hat{x}}, \quad M_{\pm}(\hat{x}, \hat{t}) = \pm \hat{s}(\hat{x})\hat{P}_{\pm}(\hat{x}, \hat{t}),$$

we arrive at the telegraph equations:

$$\begin{cases} \frac{\partial^2}{\partial \hat{t}^2}M_+(y, \hat{t}) + 2F\frac{\partial}{\partial \hat{t}}M_+(y, \hat{t}) = \frac{\partial^2}{\partial y^2}M_+(y, \hat{t}) \\ \frac{\partial^2}{\partial \hat{t}^2}M_-(y, \hat{t}) + 2F\frac{\partial}{\partial \hat{t}}M_-(y, \hat{t}) = \frac{\partial^2}{\partial y^2}M_-(y, \hat{t}) \end{cases}. \tag{3.7}$$

on a periodic boundary domain in $y \in [0, l]$, with initial values

$$M_{\pm}(y, 0) = \pm \hat{s}(y)\hat{P}_{\pm}(y, 0). \tag{3.8}$$

The initial conditions $\frac{\partial M_\pm}{\partial \hat{t}}(y,0)$ can be derived similarly from (3.3):

$$\begin{cases} \frac{\partial M_+}{\partial \hat{t}}(y,0) = -\frac{\partial M_+}{\partial y}(y,0) - F\left(M_-(y,0) + M_+(y,0)\right) \\ \frac{\partial M_-}{\partial \hat{t}}(y,0) = \frac{\partial M_-}{\partial y}(y,0) - F\left(M_+(y,0) + M_-(y,0)\right) \end{cases}. \tag{3.9}$$

The telegraph equation was historically developed to model the voltage change for long distance transmission through wire. It also describes the damped vibration of a string in a medium, where F is the damping factor (Kolesnik, 2018). The original Goldstein-Kac model is commonly written in its telegraph form to compute its analytical solution (Goldstein, 1951; Kaplan et al., 1964; Hillen, 2002; Hillen and Painter, 2009).

From the telegraph equation, we can readily compute the analytical solution $M_\pm(y,\hat{t})$ of (3.7-3.9) by Fourier series. To recover $\hat{P}_\pm(\hat{x},\hat{t})$ from $M_\pm(y,\hat{t})$ we need to do the following:

1. Compute $M_\pm(\hat{x},\hat{t})$ from $M_\pm(\hat{y},\hat{t})$ by mapping values from y to $\hat{x}$.
2. Compute $\hat{P}_\pm(\hat{x},\hat{t}) = \frac{M_\pm(\hat{x},\hat{t})}{\hat{s}(\hat{x})}$.

3.1.2 Fourier Series Solution

Suppose the solution of (3.7-3.9) with the periodic boundary conditions has the form in Fourier series

$$M_\pm(y,\hat{t}) = \sum_{n=-\infty}^{\infty} C_n^\pm(\hat{t}) e^{\frac{2\pi i n y}{l}}. \tag{3.10}$$

Substituting into (3.7) we get the relation in $C_n^\pm(\hat{t})$:

$$\frac{d^2}{d\hat{t}^2}C_n^\pm(\hat{t}) + 2F\frac{d}{d\hat{t}}C_n^\pm(\hat{t}) + \left(\frac{2\pi n y}{l}\right)^2 C_n^\pm(\hat{t}) = 0.$$

Then

$$C_n^\pm(\hat{t}) = A_n^\pm e^{(-F+R_n)\hat{t}} + B_n^\pm e^{(-F-R_n)\hat{t}}, \tag{3.11}$$

with

$$R_n = \sqrt{F^2 - \frac{4\pi^2 n^2}{l^2}}.$$

Suppose $M_{\pm}(y,0)$ and $M_{\hat{t}}^{\pm}(y,0)$ have their n-th Fourier coefficients as $U_n^{\pm}$ and $W_n^{\pm}$ defined respectively:

$$U_n^{\pm} = \frac{1}{l}\int_0^l M_{\pm}(y,0)e^{-\frac{2\pi i n y}{l}}dy, \quad W_n^{\pm} = \frac{1}{l}\int_0^l M_{\hat{t}}^{\pm}(y,0)e^{-\frac{2\pi i n y}{l}}dy,$$

then using the initial conditions $M_{\pm}(y,0)$ and $M_{\hat{t}}^{\pm}(y,0)$ we arrive at

$$A_n^{\pm} = \frac{(F+R_n)U_n^{\pm} + W_n^{\pm}}{2R_n}, \quad B_n^{\pm} = -\frac{(F-R_n)U_n^{\pm} + W_n^{\pm}}{2R_n}.$$

Fig. 3.2 is the plot of the Fourier series solution together with the corresponding Monte-Carlo simulation result. We will talk more about the details of implementing the Monte-Carlo simulation in Sec. 4.1.2.

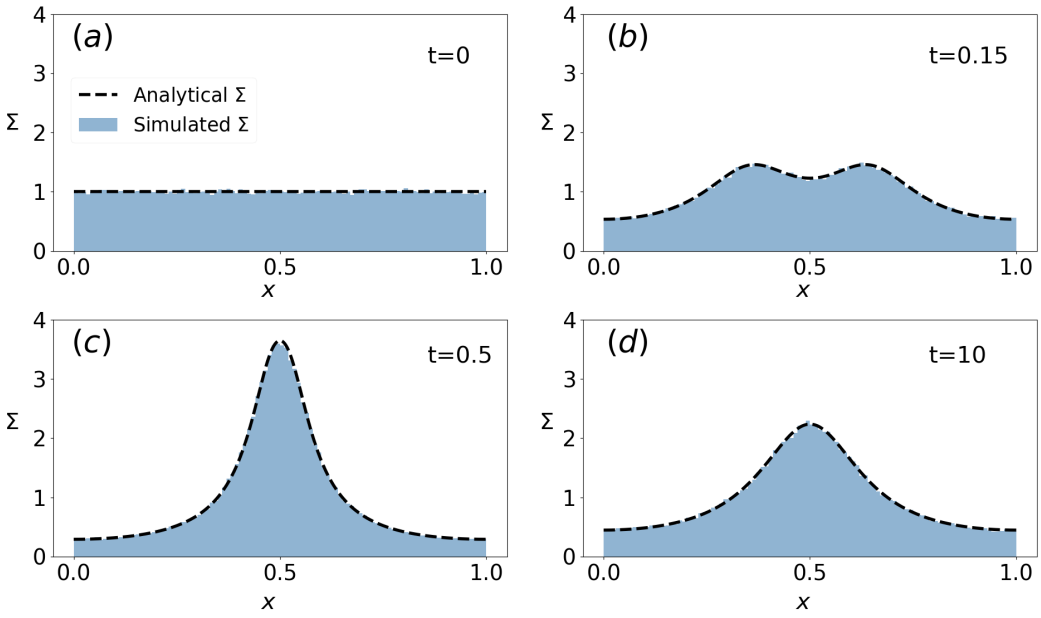

Figure 3.2: The blue histograms represent the results from an agent-based Monte-Carlo simulation with 500000 agents and the black dashed lines stand for the Fourier series solution with the same set of model parameters. Here $\Sigma = P_+ + P_-$, $s(x) = \cos(2\pi x) + 1.5$ for $x \in [0,1]$, $F = 1$. The initial condition is $P_+(x,0) = P_-(x,0) = 0.5$. At the center of the domain the smaller value of $s(x)$ represents a higher concentration of toxin, resulting in a higher density of prey.

Indeed, at steady-state, we observe that the presence of toxin leads to the aggregation of prey around the predator position. Moreover, reading from its Fourier series

solution, the steady-state distribution of the prey is fully characterized by $\hat{s}(\hat{x})$, regardless of the initial condition. In reality, this effect suggests that Karlotoxin, secreted by a stationary predator, is able to aggregate the prey around the predator.

3.2 Modeling a Translating Toxin Field

We solved for the case when the toxin field is stationary. In reality, toxin particles are secreted from the predator and they diffuse and decay in the environment. As a reminder, in our case, we are interested when the predator moves at a constant speed in a periodic domain, and the toxin concentration at steady state follows from (2.15):

$$0 = \kappa c'' + c' - \beta c + \delta(x - \gamma), \tag{3.12}$$

with the periodic solution $c(x)$:

$$c(x) = \sum_{n=-\infty}^{\infty} c_u(x + n), \quad x \in [0, 1], \tag{3.13}$$

where $c_u(x)$ is the unbounded domain solution:

$$c_u(x) = \frac{-e^{r_1(x-\gamma)}(1 - H(x - \gamma)) - e^{r_2(x-\gamma)}(1 - H(\gamma - x))}{\sqrt{1 + 4\beta\kappa}}. \tag{3.14}$$

As a reminder,

$$r_1 = \frac{-1 + \sqrt{1 + 4\beta\kappa}}{2\kappa}, \quad r_2 = \frac{-1 - \sqrt{1 + 4\beta\kappa}}{2\kappa}.$$

After the Galilean translation $x \hookleftarrow x - t$ and non-dimensionalization of (2.4) following Table 2.1, we arrive at the Goldstein-Kac system for a moving predator at constant speed 1 to the right:

$$\begin{cases} \frac{\partial P_+}{\partial t}(x, t) + \frac{\partial}{\partial x}[(s(x) - 1)P_+] = P_- - P_+ \\ \frac{\partial P_-}{\partial t}(x, t) - \frac{\partial}{\partial x}[(s(x) + 1)P_-] = P_+ - P_-. \end{cases} \tag{3.15}$$

In Fig. 2.2 we notice that $c(x)$ has a single local maximum in the domain, representing the spike of concentration of Karlotoxin. Following our general assumption that $s'(c) < 0$ (i.e., toxin slows down prey) with smooth $s(c)$, we expect to see local

minimum of $s(x)$. It turned out that whether $s(x) - 1$, the relative swimming speed of predator and prey, has roots, greatly affects how the system behaves, and changes the nature of the PDE system (3.15). For example, when $s - 1$ has roots, the system is not strictly hyperbolic. We need to further divide our discussion into the following two subcases: whether the relative speed $s - 1$ has roots, or not.

3.2.1 Steady-State when the Relative Speed Has No Roots

Suppose the relative speed $s(x) - 1$ has no roots. Note that since we imposed $s(x)$ to be continuous, we must have either $s - 1 > 0$ or $s - 1 < 0$ throughout the domain.

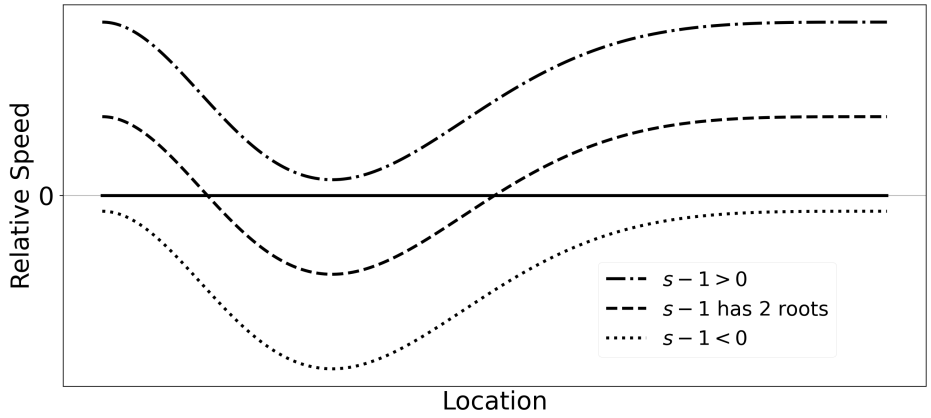

Figure 3.3: The 3 possible cases for $s - 1$: $s - 1 > 0$, $s - 1$ has 2 roots, and $s - 1 < 0$.

3.2.1.1 Characteristic Curves

We rewrite (3.15) in the following form:

$$\begin{cases} \frac{\partial P_+}{\partial t} + (s-1)\frac{\partial P_+}{\partial x} = P_- - (1+s')P_+ \\ \frac{\partial P_-}{\partial t} + (-s-1)\frac{\partial P_-}{\partial x} = P_+ - (1-s')P_-. \end{cases} \tag{3.16}$$

Note that the system is in the form of

$$\frac{\partial}{\partial t}\mathbf{P} + \Lambda(x)\frac{\partial}{\partial x}\mathbf{P} = S(\mathbf{P}), \quad \mathbf{P} = \begin{bmatrix} P_+ \\ P_- \end{bmatrix}, \tag{3.17}$$

for some operator S, where $\Lambda(x)$ is diagonal and non-singular across the domain, i.e., this system is already in its characteristic form (Bastin and Coron, 2016). In our case:

$$\Lambda(x) = \begin{bmatrix} s(x) - 1 & 0 \\ 0 & -s(x) - 1 \end{bmatrix}. \tag{3.18}$$

Therefore, the characteristic curves $t(x)$ are simply solutions of the following ODEs:

$$\frac{dt}{dx} = \frac{1}{s(x) - 1}, \quad \text{for } P_+, \tag{3.19}$$

$$\frac{dt}{dx} = -\frac{1}{s(x) + 1}, \quad \text{for } P_-. \tag{3.20}$$

We plot them in Fig. 3.4 and Fig. 3.5.

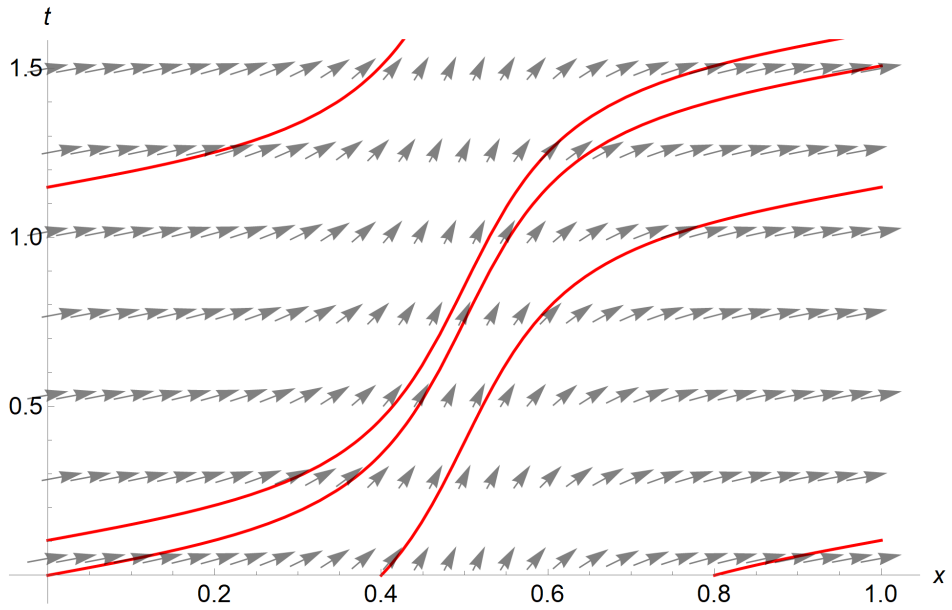

Figure 3.4: The vector field and associated various solutions for the ODE $\frac{dt}{dx} = \frac{1}{s(x)-1}$, where $s(x) - 1 > 0$. This plot corresponds to the characteristics of P_+. The magnitude of a vector is represented by its length in our example.

From an individual swimmer's point of view, the swimmer follows one characteristic curve $(x, t(x))$ in its run phase. This can be used to formulate an agent-based simulation, as used by Fok et al. (2015). Since $\pm s - 1$ has no roots, we can apply

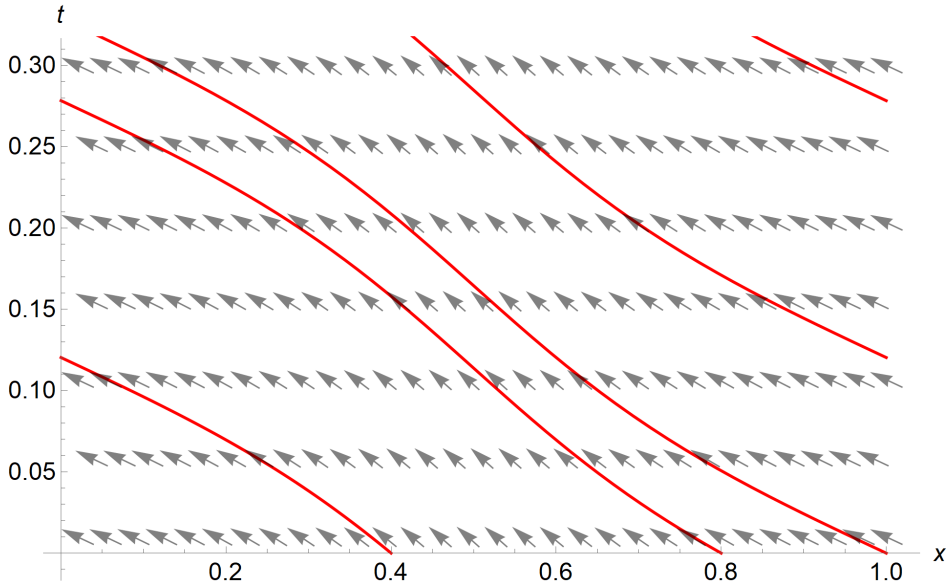

Figure 3.5: The vector field and associated various solutions for the ODE $\frac{dt}{dx} = -\frac{1}{s(x)+1}$, where $s(x) - 1 > 0$. This plot corresponds to the characteristics of P_-.

domain mapping instead by calculating the characteristics of $P_\pm$ starting at $x = 0$. That is,

$$\int_0^x \frac{1}{s(z) - 1} dz, \quad \int_x^1 \frac{1}{-s(z) - 1} dz, \tag{3.21}$$

are well defined for $x \in [0, 1]$. This is the key for a faster Monte-Carlo by avoiding calculating the characteristics at every step.

We notice that the characteristic curves are well behaved: $\frac{dt}{dx}$ is bounded, single-signed, and the solutions $t(x)$ do not cross or originate from the same point, thus contributing to no shocks or rarefactions waves. This is because $s(x)$ satisfies **(s1)**-**(s2)** and we assumed $s - 1 > 0$. Also $\frac{dt}{dx}$ is only a function of x, hence all solutions $t(x)$ from the ODE are the same shape but shifted vertically in t. The numerical algorithms also benefit from the well-behaved characteristics: Monte-Carlo and finite difference schemes both work well.

3.2.1.2 Analytical Solution

To understand this system at steady-state, we transform it by adding and subtracting the two equations in (3.15). Defining

$$\Sigma = P_+ + P_-, \tag{3.22}$$

$$\Delta = P_+ - P_-, \tag{3.23}$$

we get

$$\begin{cases} \frac{\partial \Sigma}{\partial t}(x,t) + \frac{\partial}{\partial x}(s\Delta - \Sigma) = 0 \\ \frac{\partial \Delta}{\partial t}(x,t) + \frac{\partial}{\partial x}(s\Sigma - \Delta) = -2\Delta. \end{cases} \tag{3.24}$$

We will focus on the steady-state solution of (3.15):

$$\frac{\partial}{\partial x}(s\Delta - \Sigma) = 0, \tag{3.25}$$

$$\frac{\partial}{\partial x}(s\Sigma - \Delta) = -2\Delta. \tag{3.26}$$

Further denote

$$\eta = s\Delta - \Sigma, \tag{3.27}$$

$$\xi = s\Sigma - \Delta. \tag{3.28}$$

From (3.23, 3.26) we deduce

$$\xi' + \frac{2\xi}{s^2 - 1} = -\frac{2\eta s}{s^2 - 1}. \tag{3.29}$$

Thus

$$\xi(x) = -\frac{2\eta}{\mu(x)} \int_0^x \frac{s(z)\mu(z)}{s^2(z) - 1} dz + \frac{a}{\mu(x)}, \tag{3.30}$$

where a is a constant coming from integration, and

$$\mu(x) = \exp\left[\int_0^x \frac{2}{s^2(z) - 1} dz\right]. \tag{3.31}$$

Note that μ and ξ are well-defined since $s(x) - 1$ is single-signed. From (3.27, 3.28) we have the solution:

$$\Sigma(x) = \frac{1}{2}\left(\frac{\xi(x)+\eta}{s(x)-1} + \frac{\xi(x)-\eta}{s(x)+1}\right), \tag{3.32}$$

$$\Delta(x) = \frac{1}{2}\left(\frac{\xi(x)+\eta}{s(x)-1} - \frac{\xi(x)-\eta}{s(x)+1}\right), \tag{3.33}$$

$$P_+(x) = \frac{\xi(x)+\eta}{2(s(x)-1)}, \tag{3.34}$$

$$P_-(x) = \frac{\xi(x)-\eta}{2(s(x)+1)}. \tag{3.35}$$

Here the two constants η and a can be determined by enforcing the normalizing condition $\int_0^1 \Sigma dx = 1$, and the periodic boundary condition that implies $\xi(0) = \xi(1)$. We have now found the steady-state probability density distribution for $P_\pm$. Further, we infer that the steady-state is independent from the initial conditions $P_\pm(x, t = 0)$.

3.2.1.3 Discussion

At first we should notice that $\mu(x)$ is always finite under our assumption of $s-1$ according to (3.31). Therefore $\xi(x)$ is also always finite according to (3.30), and hence $P_\pm$ are finite at steady-state, meaning there is no blow-up under our assumption of $s(x) - 1 \neq 0$.

Secondly, we apply part of Theorem A.4. in the book by Bastin and Coron (2016) to our case to show that the steady-state solution we found exists and is unique:

Theorem (Well-posedness of the Problem)**.** For every initial condition in $L^2[0, 1]$, with periodic boundary conditions, the problem (3.17) has one and only one $L^2[0, 1]$ solution.

In conclusion, the steady-state solution we constructed is unique, finite, and achievable with any L^2 initial conditions.

3.2.2 Steady-State when the Relative Speed Has Roots

Note that $\mu(x)$ in (3.31) may not be well defined at the roots of $s(x) - 1$, since $\frac{1}{s^2(x)-1}$ in the integrand is singular. From now on, we restrict our discussion to $s(x) - 1$ having two roots. Because we enforce periodicity on s, in effect one root becomes a "source" and the other a "sink" based on the relative speed's derivative as shown in Fig 3.6.

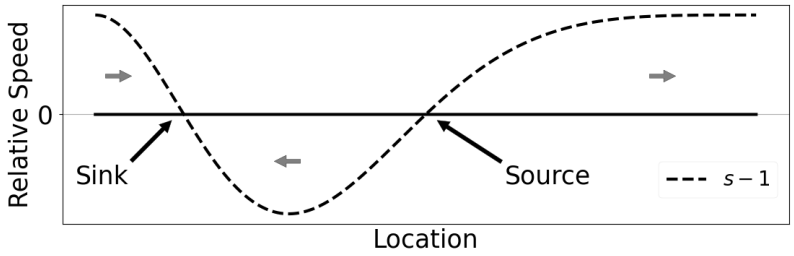

Figure 3.6: A "sink" type singularity corresponds to a downward simple crossing of the relative speed through the x-axis. Similarly, a "source" type singularity comes from an upward simple crossing. The grey arrows represent the direction of the relative speed within each region. In the absence of direction changes, a swimmer following this relative speed would get permanently trapped around the sink, and the source would have its local population density decrease to 0.

These roots introduce singularities into the model. As a result, for analytical solutions, we cannot use the same solution procedure as in Sec. 3.2.1.2. Also the source root in $s - 1$ leads to poor convergence for our agent-based Monte-Carlo simulations, to a point that we will not use them to verify our analysis. This poor performance is explained in detail in Sec. 4.1.3.

3.2.2.1 Characteristic Curves

Similar to Sec. 3.2.1.1, we rewrite (3.15) into the following form:

$$\frac{\partial}{\partial t}\mathbf{P} + \Lambda(x)\frac{\partial}{\partial x}\mathbf{P} = \begin{bmatrix} -1 - s' & 1 \\ 1 & -1 + s' \end{bmatrix} \mathbf{P},$$

however

$$\Lambda(x) = \begin{bmatrix} s(x) - 1 & 0 \\ 0 & -s(x) - 1 \end{bmatrix} \tag{3.36}$$

is singular at the roots, indicating that the system is not strictly hyperbolic. We plot the characteristic curves in Fig. 3.7 and Fig. 3.8. We conclude the following from the characteristic curves:

1. The characteristics do not necessarily merge with the sink in infinite time. For some choice of $s(x)$, the time taken to arrive at the sink for a swimmer is finite: Denote the sink location as x_1, the source location as x_3. Since $\frac{dt}{dx} = \frac{1}{s(x)-1}$, for a characteristic curve starting at x_s that is not the sink or the source, the characteristic merges with x_1 in finite time if and only if $t(x_1) = \int_{x_s}^{x_1} \frac{1}{s(x)-1} dx$ converges.

2. We cannot conclude just from Fig. 3.7 that all the swimmers will aggregate near the sink eventually as compared to 3.4, since it is only for P_+, and the characteristic curves do not consider the direction switches. However, the difference between Fig. 3.7 and Fig. 3.4 is from the direction change of flux at x_1 and x_3, which does need to be taken into account when designing finite difference schemes. See Sec. 4.2 for the details.

3. In contrast, P_- is always well-behaved: $\frac{dt}{dx}$ is bounded, single-signed, and the solutions $t(x)$ do not cross or originate from the same point. Indeed, in its steady-state, P_+ at the sink can have an integrable singularity, while P_- always stays finite across the domain. We will discuss the solutions in detail in Sec. 3.2.2.5.

3.2.2.2 The Method of Frobenius

In our case, the PDE system (3.15) is no longer hyperbolic under the presence of roots for $s(x) - 1$. Thus most analysis tools designed for hyperbolic systems no longer work, however the method of Frobenius still allows one to construct series solutions locally for our ODE system. We list several key results from the method of Frobenius in this section. Those results are crucial for understanding the local behavior of our system

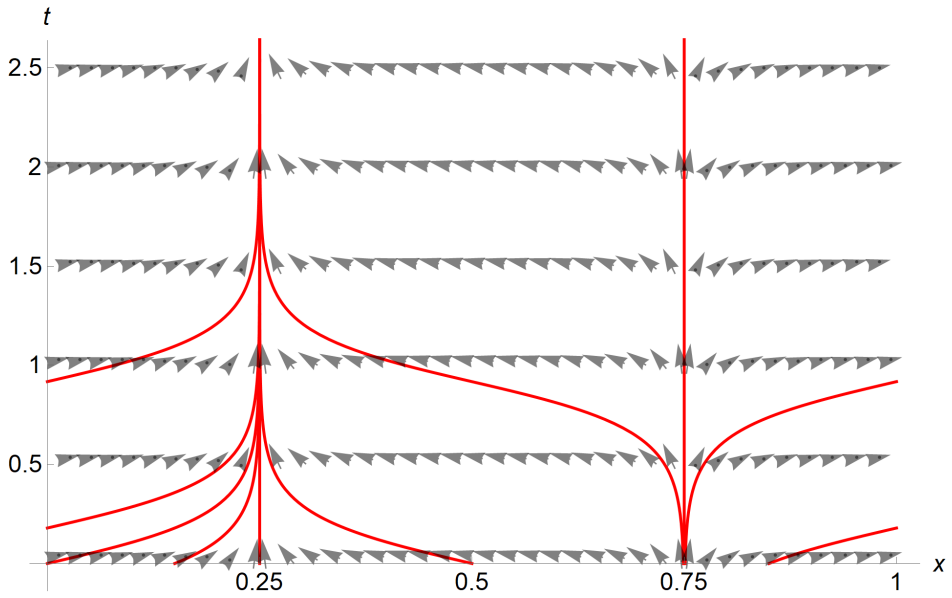

Figure 3.7: The vector field and associated various solutions for the ODE $\frac{dt}{dx} = \frac{1}{s(x)-1}$, where $s(x) - 1$ has two roots at 0.25 (the sink) and 0.75 (the source). This plot corresponds to the characteristics of P_+. At 0.25 and 0.75 the solutions are vertical lines. Note the three curves seemingly starting at 0.75 actually start at $0.74999, 0.75, 0.75001$ respectively, and they diverge quickly.

around the roots of the relative speed. Specifically, conclusions from the Frobenius analysis are necessary in our construction of the steady-state analytical solution for the system. Holubec and Stauffer (1985) and Howell (2019) gave the full details of the method of Frobenius in the complex domain with iterative formulas on calculating all the unknown coefficients. We adapt those to our case. With the method of the Frobenius, one could construct a full series solution for the ODEs that correspond to the steady-state of our Goldstein-Kac system, though such a solution needs to take the radius of convergence into account. For this reason, we do not choose the series solutions from the method of Frobenius as our analytical solution for the system (3.15).

Suppose we have the following general second order linear ODE:

$$\mathcal{L}[y] = (x - x_0)^2 y'' + (x - x_0)\alpha(x)y' + \beta(x)y = 0, \tag{3.37}$$

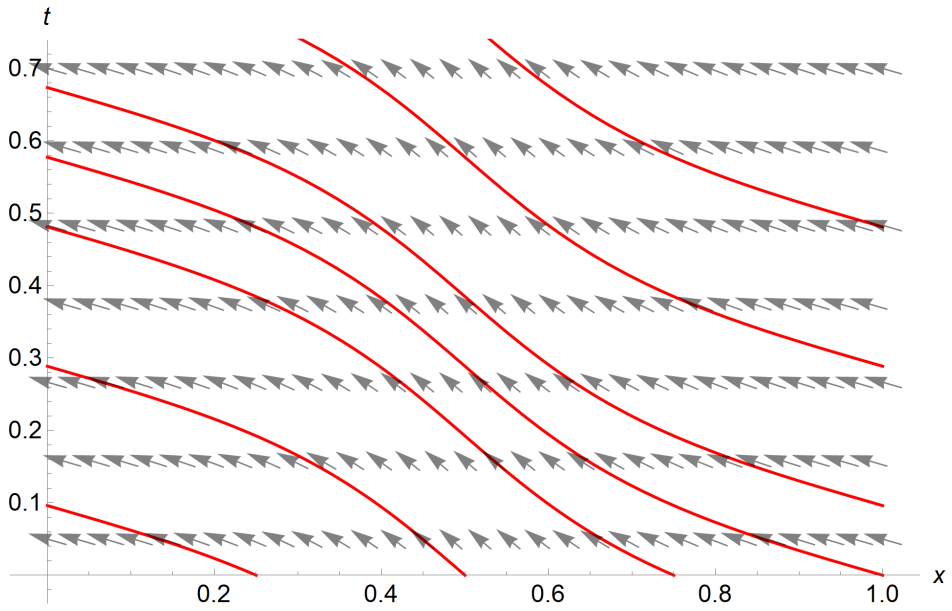

Figure 3.8: The vector field and associated various solutions for the ODE $\frac{dt}{dx} = -\frac{1}{s(x)+1}$, where $s(x) = \cos(2\pi x) + 1$. This plot corresponds to the characteristics of P_-. In contrast to P_+ as seen in Fig. 3.7, the characteristics of P_- are in the same direction with bounded slope.

with $\alpha(x), \beta(x)$ being analytic at x_0, i.e.,

$$\alpha(x) = \sum_{k=0}^{\infty} \alpha_k (x - x_0)^k,$$
$$\beta(x) = \sum_{k=0}^{\infty} \beta_k (x - x_0)^k.$$

In this case, we call x_0 a regular singular point for (3.37). We then obtain the indicial equation $I(\sigma) = 0$ by plugging the following Frobenius series

$$y(x) = |x - x_0|^{\sigma} \sum_{k=0}^{\infty} c_k (x - x_0)^k, \quad c_0 = 1, \tag{3.38}$$

for some constant σ into (3.37), then take $k = 0$:

$$I(\sigma) = \sigma(\sigma - 1) + \alpha_0 \sigma + \beta_0 = 0 \tag{3.39}$$

The two roots σ_1, σ_2 can be the same. For our analysis in finding the steady-state distribution of population densities, we will see that $\sigma_1, \sigma_2 \in \mathbb{R}$ because $\beta_0 = 0$ in (3.64), hence we can further impose $\sigma_1 \geq \sigma_2$ without loss of generality.

Theorem (The Method of Frobenius)**.** The general solution to the differential equation $\mathcal{L}[y] = 0$ (3.37) around x_0 is

$$y(x) = l_1 y_1(x) + l_2 y_2(x) \tag{3.40}$$

with arbitrary constants l_1, l_2. $y_1(x)$ always has the Frobenius series form:

$$y_1(x) = |x - x_0|^{\sigma_1} \sum_{k=0}^{\infty} a_k (x - x_0)^k, \quad a_0 = 1, \tag{3.41}$$

and $y_2(x)$ must come from one of the three cases listed below:

1. $\sigma_1 - \sigma_2 \notin \mathbb{Z}$, then

$$y_2(x) = |x - x_0|^{\sigma_2} \sum_{k=0}^{\infty} b_k (x - x_0)^k, \quad b_0 = 1. \tag{3.42}$$

   This is the nice case where both y_1 and y_2 are in the form of Frobenius series.

2. $\sigma_1 = \sigma_2$, then

$$y_2(x) = y_1(x) \ln|x - x_0| + |x - x_0|^{1+\sigma_1} \sum_{k=0}^{\infty} b_k (x - x_0)^k, \quad b_0 = 1. \tag{3.43}$$

3. $\sigma_1 - \sigma_2 = Z$ for a positive integer Z, then

$$y_2(x) = K y_1(x) \ln|x - x_0| + |x - x_0|^{\sigma_2} \sum_{k=0}^{\infty} b_k (x - x_0)^k, \quad b_0 = 1. \tag{3.44}$$

   For the coefficients in (3.44): K is a constant that can be calculated from b_k's for $k < Z$, and might be 0. $b_0, b_1, \cdots, b_{Z-1}$ are determined, however, b_Z is arbitrary (Often people simply set $b_Z = 0$.) and as a result the value of b_k for $k > Z$ depends on the choice of b_Z.

The detailed derivation of the method of Frobenius can be found in Chapter 37 of the book by Howell (2019).

3.2.2.3 Iterative Formulas for Coefficients

We now demonstrate how to calculate the coefficients for the solutions obtained from the method of Frobenius for all 3 cases. We present the iterative formulas only, and the justification is provided also in Chapter 37 of the book by Howell (2019).

Case 1 Here $\sigma_1 - \sigma_2 \notin \mathbb{Z}$. All coefficients a_k, b_k for $y_1(x), y_2(x)$ respectively can be iteratively calculated from series coefficients of α, β. Generally, for a Frobenius series of form $|x - x_0|^\sigma \sum_{k=0}^{\infty} c_k (x - x_0)^k$, the iterative formula for the coefficient c_k is

$$c_k = \frac{-1}{I(k+\sigma)} \sum_{j=0}^{k-1} c_j [\alpha_{k-j}(j+k) + \beta_{k-j}], \quad k = 1, 2, \cdots. \tag{3.45}$$

Remark: For both case 2 and 3, the iterative formula for a_k still follows (3.45). However the iterative formulas for b_k in case 2 and a subcase of case 3 require us to calculate $\epsilon(x)$ that comes from the proposed solution form

$$y_2(x) = y_1(x) \ln|x - x_0| + \epsilon(x). \tag{3.46}$$

Case 2 Here $\sigma_1 = \sigma_2$. We know from (3.43)

$$\epsilon(x) = |x - x_0|^{1+\sigma_1} \sum_{k=0}^{\infty} b_k (x - x_0)^k. \tag{3.47}$$

Define

$$f_k = -2(k+1)a_{k+1} - \sum_{j=0}^{k} a_j \alpha_{k+1-j}. \tag{3.48}$$

The iterative formula for coefficients b_k of $\epsilon(x)$ is given by

$$\begin{aligned} b_0 &= f_0, \\ b_k &= \frac{1}{(k+1)^2} \left(f_k - \sum_{j=0}^{k-1} b_j [\alpha_{k-j}(j + \sigma_1 + 1) + \beta_{k-j}] \right), \quad k > 0. \end{aligned} \tag{3.49}$$

Case 3 Here $\sigma_1 - \sigma_2 = Z$. Introduce a constant Γ_Z below. First calculate the coefficients b_k iteratively for $k = 0, 1, 2, \cdots, Z - 1$ via

$$\begin{aligned} b_0 &= 1, \\ b_k &= \frac{-1}{I(\sigma_2 + k)} \sum_{j=0}^{k-1} b_j [\alpha_{k-j}(j + \sigma_2) + \beta_{k-j}]. \end{aligned} \tag{3.50}$$

Then we calculate Γ_Z as

$$\Gamma_Z = \sum_{j=0}^{Z-1} b_j[\alpha_{Z-j}(\sigma_2 + j) + \beta_{Z-j}]. \tag{3.51}$$

It can be shown that

$$K = -\frac{\Gamma_Z}{Z}, \tag{3.52}$$

and the formula for $\epsilon(x)$ has two subcases depending on whether $\Gamma_Z = 0$:

If $\Gamma_Z = 0$, then $K = 0$, and y_2 is directly given by the Frobenius series form below instead of (3.46):

$$y_2(x) = |x - x_0|^{\sigma_2} \sum_{k=0}^{\infty} b_k (x - x_0)^k, \tag{3.53}$$

and the coefficients can be calculated via the generic iterative formula (3.45). Moreover, b_Z is arbitrary, and one can simply let $b_Z = 0$.

If $\Gamma_Z \neq 0$, then it can be shown that y_2 still follows (3.46):

$$y_2(x) = y_1(x) \ln|x - x_0| + \epsilon(x).$$

This is equivalent to dividing the form of $y_2(x)$ given in (3.44) by K, since $K \neq 0$ from (3.52). Thus denote $\epsilon_k = \frac{b_k}{K}$ and we get

$$\epsilon(x) = |x - x_0|^{\sigma_2} \sum_{k=0}^{\infty} \epsilon_k (x - x_0)^k. \tag{3.54}$$

Define

$$f_k = a_{k-Z}(Z - 2k) - \sum_{j=0}^{k-Z-1} a_j \alpha_{k-Z-j}, \quad k > Z. \tag{3.55}$$

The iterative formula for ϵ_k is given as

$$\begin{aligned}
\epsilon_0 &= -\frac{Z}{\Gamma_Z}, \\
\epsilon_k &= \frac{-1}{I(\sigma_2 + k)} \sum_{j=0}^{k-1} \epsilon_j[\alpha_{k-j}(\sigma_2 + j) + \beta_{k-j}], \quad 0 < k < Z, \\
\epsilon_k &= \frac{1}{I(\sigma_2 + k)} \left(f_k - \sum_{j=0}^{k-1} \epsilon_j[\alpha_{k-j}(\sigma_2 + j) + \beta_{k-j}] \right), \quad k > Z.
\end{aligned} \tag{3.56}$$

Finally

$$b_k = K\epsilon_k. \tag{3.57}$$

Still, b_Z is arbitrary, and we can let $b_Z = 0$ without loss of generality. Overall for case 3 where $\sigma_1 - \sigma_2 = Z$, K is a constant that can be computed from Γ_Z, and it might be 0.

3.2.2.4 Local Analysis with the Method of Frobenius

System (3.15) in its steady-state can be decoupled as follows:

$$P_+''(x) + \frac{p_+(x)}{x - x_i} P_+'(x) + \frac{q_+(x)}{(x - x_i)^2} P_+(x) = 0, \tag{3.58}$$

$$P_-''(x) + \frac{p_-(x)}{x - x_i} P_-'(x) + \frac{q_-(x)}{(x - x_i)^2} P_-(x) = 0, \tag{3.59}$$

where

$$p_\pm(x) = \frac{2 \pm s' + 3ss'}{s^2 - 1}(x - x_i) = \sum_{n=0}^{\infty} p_n^\pm (x - x_i)^n, \tag{3.60}$$

$$q_\pm(x) = \frac{(s')^2 + (\pm 1 + s)s''}{s^2 - 1}(x - x_i)^2 = \sum_{n=1}^{\infty} q_n^\pm (x - x_i)^n, \tag{3.61}$$

and $x_i = x_1, x_3$, defined as the only two roots of $s - 1$. Specifically x_1 is a sink and x_3 is a source. Notice

$$s - 1 = s'(x_i)(x - x_i) + O(x - x_i)^2. \tag{3.62}$$

As a reminder, x_1 and x_3 are simple zeros of $s - 1$, hence $s'(x_i) \neq 0$. Therefore $p_\pm(x)$ and $q_\pm(x)$ have removable singularities at $x = x_1$ and $x = x_3$, and (3.58, 3.59) both have at worst regular singular points at $x = x_i$. We carry out the examination for P_+ below, and the case for P_- follows similarly.

At x_i, at least one solution for (3.58) is in the Frobenius form

$$P_+ = (x - x_i)^\sigma T(x) \tag{3.63}$$

for some constant σ and normalized Taylor series $T(x)$ with constant term 1. The other solution may also follow the Frobenius form, or exhibit a logarithmic structure

(Holubec and Stauffer 1985). Thus, by expanding p_+, q_+ into Taylor series around $x = x_i$ we find that the indicial equation for (3.58) is

$$\sigma^2 + (p_0^+ - 1)\sigma = 0, \quad \text{with } p_0^+ = \frac{1}{s'(x_i)} + 2. \tag{3.64}$$

Denote

$$\nu(x_i) = -\frac{1}{s'(x_i)}. \tag{3.65}$$

This important non-dimensional quantity will appear frequently for the rest of our analysis. Similarly, the indicial equation for (3.59) is

$$\sigma^2 + (p_0^- - 1)\sigma = 0, \quad \text{with} \quad p_0^- = \frac{1}{s'(x_i)} + 1. \tag{3.66}$$

The characteristic roots for $P_\pm$ from the indicial equations are therefore

$$\sigma_1 = 0, \quad \sigma_2 = \nu(x_i) - 1, \quad \text{for } P_+, \tag{3.67}$$

$$\sigma_1 = 0, \quad \sigma_2 = \nu(x_i), \quad \text{for } P_-. \tag{3.68}$$

The root at 0 represents a regular Taylor series expansion around x_i which is referred as the regular branch. This solution in the form of Frobenius series always exists. The branch corresponding to the other root needs to be discussed in different cases depending on σ_2.

We denote all normalized Taylor series in the form of $T^{\pm}_{j,i}(x)$. Here j is an index for distinguishing purpose, $i \in \{1, 3\}$ indicates if it is used near x_1 or x_3, and the $\pm$ sign indicates if it is used for P_+ or P_-.

At x_1, for $\nu(x_1) \notin \mathbb{Z}$:

$$P_+(x) = G^+_{1,1}T^+_{1,1}(x) + |x - x_1|^{\nu(x_1)-1}G^+_{2,1}T^+_{2,1}(x), \tag{3.69}$$

$$P_-(x) = G^-_{1,1}T^-_{1,1}(x) + |x - x_1|^{\nu(x_1)}G^-_{2,1}T^-_{2,1}(x). \tag{3.70}$$

At x_3, for $\nu(x_3) \notin \mathbb{Z}$:

$$P_+(x) = G^+_{1,3}T^+_{1,3}(x) + |x - x_3|^{\nu(x_3)-1}G^+_{2,3}T^+_{2,3}(x), \tag{3.71}$$

$$P_-(x) = G^-_{1,3}T^-_{1,3}(x) + |x - x_3|^{\nu(x_3)}G^-_{2,3}T^-_{2,3}(x), \tag{3.72}$$

with constants $G^{\pm}_{j,i}$. Their notation consensus is consistent with that of $T^{\pm}_{j,i}(x)$.

1. At x_1, $s'(x_1) < 0$ so $\nu(x_1) > 0$. Therefore P_+ has at worst an integrable singularity at $x = x_1$. P_+ is continuous if $-1 < s'(x_1) < 0$ (i.e., $\nu(x_1) > 1$).

2. At x_3, $s'(x_3) > 0$ then $\nu(x_3) - 1 < -1$ and $\int_0^1 P_+ dx$ will be undefined for $G^+_{2,3} \neq 0$. Therefore we must take

$$G^+_{2,3} = 0. \tag{3.73}$$

Using the relation

$$\eta = s\Delta - \Sigma = (s-1)P_+ - (s+1)P_-, \tag{3.74}$$

we have

$$P_- = \frac{-\eta}{s+1} + \frac{s-1}{s+1}P_+, \tag{3.75}$$

where η is constant throughout the domain, as discussed in Appendix A.1. Therefore, from P_+ being finite at x_3, P_- should also be finite and therefore

$$G^-_{2,3} = 0. \tag{3.76}$$

Thus, both $P_\pm$ are regular at x_3 when $\nu(x_3) \notin \mathbb{Z}$.

Now suppose $\nu(x_i) \in \mathbb{Z}$, the indicial roots $\sigma_1 - \sigma_2 \in \mathbb{Z}$ for both $P_\pm$. The Frobenius method always leads to a valid first solution in the Frobenius form (in this case a Taylor series), however the second solution requires further discussion. For all the analysis below, the normalized Taylor series $T_{j,i}$ and $T^\pm_{j,i}$ all have constant term 1 by construction:

1. At x_3, for P_+, the two roots are 0 and $\nu(x_3) - 1 < -1$. According to the method of Frobenius, P_+ can be written as a linear combination of y_1 and y_2:

$$y_1 = T_{1,3}(x),$$

$$y_2 = K y_1(x) \ln|x - x_3| + |x - x_3|^{\nu(x_3)-1} T_{2,3}(x),$$

for a known constant K (which might be 0). Since the two indicial roots are distinct, we must have $P_+(x) \propto y_1$, otherwise y_2 would not not integrable at x_3. When combined with (3.75), we can represent

$$P_+(x) = G^+_{1,3}T^+_{1,3}(x), \tag{3.77}$$

$$P_-(x) = G^-_{1,3}T^-_{1,3}(x), \tag{3.78}$$

That is, $P_\pm$ are regular around x_3 when $\nu(x_3) \in \mathbb{Z}$. Therefore $P_\pm$ near x_3 are regular for all $\nu(x_3)$. We can conclude that the prey's density function Σ near the source is always regular at steady-state.

2. At x_1 we need to further divide our discussion into 2 subcases depending on whether $\nu(x_1) - 1 = 0$ or $= 1, 2, \ldots$.

Case I : Suppose $\nu(x_1) - 1 = 0$, then for P_+ we have

$$y_1 = T_{1,1}(x), \tag{3.79}$$

$$y_2 = y_1 \ln|x - x_1| + |x - x_1|T_{2,1}(x). \tag{3.80}$$

Therefore, the solution has the form

$$P_+(x) = G^+_{1,1}T^+_{1,1}(x) + G^+_{2,1}T^+_{1,1}(x)\ln|x - x_1| + |x - x_1|G^+_{2,1}T^+_{2,1}(x). \tag{3.81}$$

And we get P_- via (3.75):

$$\begin{aligned} P_-(x) = {} & G^-_{1,1}T^-_{1,1}(x) + |x - x_1|G^-_{2,1}T^-_{1,1}(x)\ln|x - x_1| \\ & + |x - x_1|^2 G^-_{2,1}T^-_{2,1}(x). \end{aligned} \tag{3.82}$$

One may also derive (3.82) directly from the method of Frobenius without using (3.75), but it would fall into the case 3 of the method of Frobenius theorem in Sec. 3.2.2.2 and would be less specific than (3.82) by introducing a constant K, since the two indicial roots for P_- are 0 and $\nu(x_1) = 1$.

Case II : Suppose $\nu(x_1) - 1 = 1, 2, 3, \ldots$, then P_+ has two independent solutions y_1 and y_2:

$$y_1 = T_{1,1}(x), \tag{3.83}$$

$$y_2 = K y_1 \ln|x - x_1| + |x - x_1|^{\nu(x_1)-1} T_{2,1}(x), \tag{3.84}$$

for a constant K (which can be calculated and might be 0). Therefore P_+ has the form

$$\begin{aligned} P_+(x) = {} & G^+_{1,1} T^+_{1,1}(x) + K G^+_{2,1} T^+_{1,1}(x) \ln|x - x_1| \\ & + |x - x_1|^{\nu(x_1)-1} G^+_{2,1} T^+_{2,1}(x), \end{aligned} \tag{3.85}$$

and we get P_- via (3.75):

$$\begin{aligned} P_-(x) = {} & G^-_{1,1} T^-_{1,1}(x) + |x - x_1| K G^-_{2,1} T^-_{1,1}(x) \ln|x - x_1| \\ & + |x - x_1|^{\nu(x_1)} G^-_{2,1} T^-_{2,1}(x). \end{aligned} \tag{3.86}$$

Note that these terms with a logarithm component are locally integrable because the singularity is at worst $\ln(x)$.

3.2.2.5 Analytical Solution

We try to solve the ODE system (3.26, 3.25) with $s'(x_1) < 0$ and $s'(x_3) > 0$. Let x_2 be an arbitrary point such that $x_0 = 0 < x_1 < x_2 < x_3 < 1 = x_4$. The property $\int_0^1 \Sigma dx = 1$ persists, and

$$\frac{d}{dx}(s\Delta - \Sigma) = 0, \tag{3.87}$$

$$\frac{d}{dx}(s\Sigma - \Delta) = -2\Delta. \tag{3.88}$$

We start by finding the structure of ξ and its auxiliary function μ. However μ globally defined as

$$\mu(x) = \exp\left[\int_0^x \frac{2}{s^2(z) - 1} dz\right]$$

in (3.31) is no longer valid in general because we cannot integrate through singularities of $\frac{1}{s(x)-1}$ if it has a pole of order greater than or equal to 1. Therefore to find a general solution, we subdivide the domain into 4 intervals so that within each interval, $s(x)-1$ is of single sign: $I_1 = [x_0, x_1)$, $I_2 = (x_1, x_2]$, $I_3 = (x_2, x_3)$, $I_4 = (x_3, x_4]$. x_2 can be included in either I_2 or I_3, and it does not affect the analysis. We then aim to solve μ, ξ on each I_i with proper joining conditions. Note that η is constant across all the intervals as discussed in Appendix A.1.

For each i,

$$(\mu_i \xi_i)' = -\frac{2\eta s \mu_i}{s^2 - 1}. \tag{3.89}$$

Then we specify μ_i and ξ_i as follows as a generalization from Sec. 3.2.1.2:

$$\mu_i(x) = \begin{cases} \exp\left[\int_{x_{i-1}}^{x} \frac{2}{s^2(z)-1} dz\right], & i = 1, 3; \quad (3.90) \\ \exp\left[-\int_{x}^{x_i} \frac{2}{s^2(z)-1} dz\right], & i = 2, 4; \quad (3.91) \end{cases}$$

$$\xi_i(x) = \begin{cases} -\frac{2\eta}{\mu_i(x)} \int_{x_{i-1}}^{x} \frac{s(z)\mu_i(z)}{s^2(z)-1} dz + \frac{a_i}{\mu_i(x)}, & i = 1, 3; \quad (3.92) \\ \frac{2\eta}{\mu_i(x)} \int_{x}^{x_i} \frac{s(z)\mu_i(z)}{s^2(z)-1} dz + \frac{a_i}{\mu_i(x)}, & i = 2, 4. \quad (3.93) \end{cases}$$

Now from (3.92, 3.93) we have 5 unknown constants a_1, a_2, a_3, a_4 and η and hence we need to find 5 joining conditions. They are:

(**I**) $\xi(0) = \xi(1)$ since $\xi(x)$ is periodic on $[0, 1]$.

(**II**) Continuity of $\xi(x)$ at $x = x_2$, because (3.89) is regular at x_2.

(**III**) $\lim_{x \to x_3^-} \mu_3 \xi_3 = 0$.

(**IV**) $\lim_{x \to x_3^+} \mu_4 \xi_4 = 0$.

(**V**) $\int_0^1 \Sigma(x) dx = 1$, by conservation of probability.

Here (**III**) and (**IV**) are justified in Appendix A.2. Respectively, each condition can be rewritten in terms of a_1, a_2, a_3, a_4 and η.

(**i**) $a_1 = a_4$.

(**ii**) $a_2 = a_3$.

(**iii**) $a_3 = 2\int_{x_2}^{x_3^-} \frac{s(z)\mu_3(z)}{s^2(z)-1}dz$.

(**iv**) $a_4 = -2\int_{x_3^+}^{1} \frac{s(z)\mu_4(z)}{s^2(z)-1}dz$.

(**v**) $\sum_{i=1}^{4}\left[\int_{I_i}\frac{s(x)\xi_i(x)+\eta}{s^2(x)-1}dx\right] = 1$. Note that after (i)-(iv), every ξ_i has only η as the undetermined parameter.

The derivations are shown in the Appendix A.3.

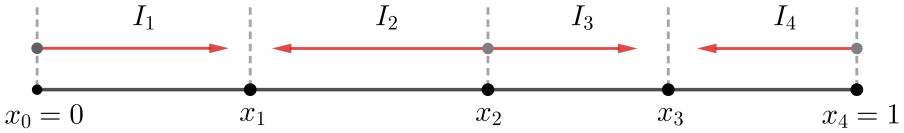

Figure 3.9: The red arrows are the directions of integration for μ_i and ξ_i within each interval I_i.

Through these conditions, we are able to calculate ξ and η, and thus $P_\pm$. With a_1-a_4 and η known, the full solution using (3.34, 3.35) is:

$$P_+ = \begin{cases} -\frac{\eta}{\mu_i(s-1)}\int_{x_{i-1}}^{x}\frac{s(z)\mu_i(z)}{s^2(z)-1}dz + \frac{a_i}{2\mu_i(s-1)} + \frac{\eta}{2(s-1)}, & \text{i = 1,3;} \quad (3.94) \\ \frac{\eta}{\mu_i(s-1)}\int_{x}^{x_i}\frac{s(z)\mu_i(z)}{s^2(z)-1}dz + \frac{a_i}{2\mu_i(s-1)} + \frac{\eta}{2(s-1)}, & \text{i = 2,4;} \quad (3.95) \end{cases}$$

$$P_- = \begin{cases} -\frac{\eta}{\mu_i(s+1)}\int_{x_{i-1}}^{x}\frac{s(z)\mu_i(z)}{s^2(z)-1}dz + \frac{a_i}{2\mu_i(s+1)} - \frac{\eta}{2(s+1)}, & \text{i = 1,3;} \quad (3.96) \\ \frac{\eta}{\mu_i(s+1)}\int_{x}^{x_i}\frac{s(z)\mu_i(z)}{s^2(z)-1}dz + \frac{a_i}{2\mu_i(s+1)} - \frac{\eta}{2(s+1)}. & \text{i = 2,4;} \quad (3.97) \end{cases}$$

3.2.2.6 Discussion

We are now able to solve for the steady-state $P_\pm(x)$ analytically given $s(x)$. Still, the steady-state distributions of $P_\pm(x)$ do not depend on the initial conditions, but the

solutions are quite different from (3.34, 3.35) when there are roots in the relative speed $s-1$.

From the method of Frobenius, when the slope of $s(x)$ at the sink is "steep", i.e., $0 < -\frac{1}{s'(x_1)} \leq 1$, it leads to an integrable singularity and therefore the global maximum in the prey's population at the sink. When the slope is "shallow", i.e., $-\frac{1}{s'(x_1)} > 1$, and $-\frac{1}{s'(x_1)} \notin \mathbb{Z}$, $P_\pm$ is bounded at steady-state, and there is a local maximum at x_1. When $-\frac{1}{s'(x_1)} > 1$ and $-\frac{1}{s'(x_1)} \in \mathbb{Z}$, one can calculate the constant K in the local solution of P_+ at x_1 given $s(x)$, and if $K \neq 0$ then there is a logarithmic singularity at x_1, otherwise not. Though from the characteristics and our numerical experiments, it is likely that $K = 0$ whenever $-\frac{1}{s'(x_1)} > 1$, which implies that likely whenever $-\frac{1}{s'(x_1)} > 1$, the prey's population is bounded at x_1. One can calculate K in this situation in a case-by-case basis using (3.51) and (3.52), however, the general proof (or disproof) of $K = 0$ is left for future work.

Also, although Σ can develop an integrable singularity, realistically it cannot happen because a few modeling assumptions can break down. For example, in reality prey have finite sizes and do not move independently. Also instant turning may not be a good approximation.

Chapter 4

NUMERICAL SIMULATIONS AND COMPUTATIONS

4.1 Monte-Carlo Simulation

In this section, we describe a Monte-Carlo method to simulate a swimmer's location whose density $P_{\pm}(x,t)$ follows the extended Goldstein-Kac system:

$$\begin{cases} \frac{\partial}{\partial t}P_{+}(x,t) + \frac{\partial}{\partial x}\left[s_{+}(x)P_{+}(x,t)\right] = F(P_{-}(x,t) - P_{+}(x,t)) \\ \frac{\partial}{\partial t}P_{-}(x,t) - \frac{\partial}{\partial x}\left[s_{-}(x)P_{-}(x,t)\right] = F(P_{+}(x,t) - P_{-}(x,t)), \end{cases} \tag{4.1}$$

where $s_{\pm}(x)$ have no roots and satisfy the regularity conditions **(s2)**, **(s3)**, and $x \in [0, L]$. We aim to compute the distribution of $P_{\pm}$ at a given time by running the simulation with large amounts of swimmers. In this system, a right-moving swimmer follows the speed $s_{+}(x)$ and a left-moving swimmer follows the speed $s_{-}(x)$. This system includes both the stationary toxin case as in Sec. 3.1, and the case when the moving predator and the prey's relative speed has no roots as in Sec. 3.2.1. Specifically, Monte-Carlo is not used when the relative speed $s - 1$ has zeros.

4.1.1 Behavior of Individual Swimmers

In this subsection, we discuss the Goldstein-Kac system from an individual swimmer's point of view, as it helps to formulate our Monte-Carlo algorithm later. Assume the following movement rule: a swimmer moves according to $s_{+}(x)$ or $s_{-}(x)$ based on its swimming direction, and changes its swimming direction instantaneously. The random time between two adjacent direction changes is drawn independently from $Exp[F]$.

In our agent-based simulation, the central issue lies in how to calculate the location of a swimmer accurately given its initial location, swimming direction, swimming

time and its swimming speed $s(x)$. We achieve this by a domain mapping between x and $y_\pm$, as discussed below.

4.1.2 Monte-Carlo Algorithm

When the relative speed has no roots, we can calculate the location of a single swimmer at a given list of observation times through a domain mapping between x and y with **Algorithm 1**. Call this list of observation times $\{t_{\text{obs}}^{(i)}\}$. Briefly speaking, the locations at the observation times are calculated as follows:

1. Generate the list of times $\{t_{\text{flip}}^{(i)}\}$ where the swimmer flips its direction.
2. Merge $\{t_{\text{obs}}^{(i)}\}$ with $\{t_{\text{flip}}^{(i)}\}$ into $\{t_{\text{merge}}^{(i)}\}$, sort and re-index. See Fig. 4.1 for an illustration.
3. Calculate the exact location x_{loc} of the swimmer at every $t_{\text{merge}}^{(i)}$. Note within any time interval $(t_{\text{merge}}^{(i-1)}, t_{\text{merge}}^{(i)})$, the swimmer does not change its direction. The final location within this time interval can be calculated exactly once the initial location, swimming time, swimming direction and swimming speed $s(x)$ are given.
4. Extract the locations at all observation times $\{x_{\text{loc}}(t_{\text{obs}}^{(i)})\}$ from the locations at the merged times $\{x_{\text{loc}}(t_{\text{merge}}^{(i)})\}$.

In the above process, step 3 computes the exact location of the swimmer at the end of each time interval through domain mapping between x and $y_\pm$ in 4 steps as illustrated in Fig. 4.2.

We repeat this agent-based process for many agents with randomized initial direction and initial location according to $P_\pm(x, t = 0)$. Then we compute the density histogram of left-moving and right-moving swimmers at each observation time in $\{t_{\text{obs}}^{(i)}\}$ to approximate $P_-(x, t)$ and $P_+(x, t)$.

Algorithm 2 includes details of generating the initial directions and locations. Briefly speaking:

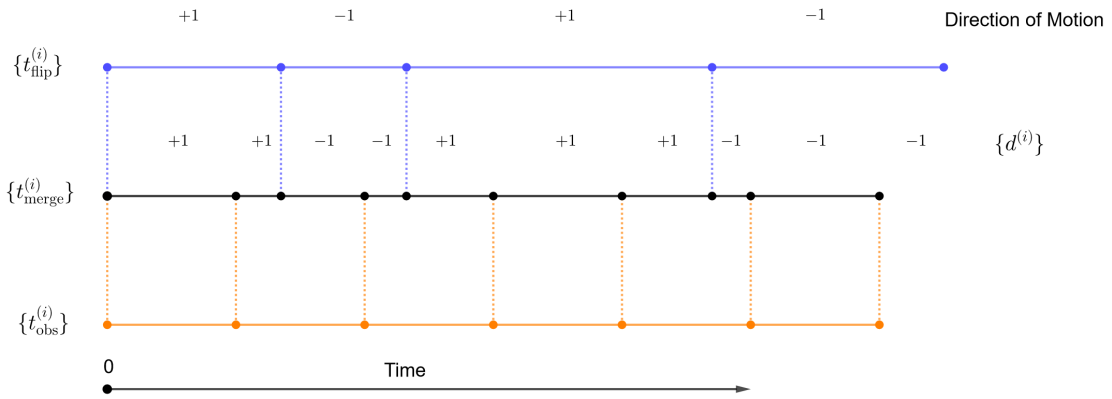

Figure 4.1: Merging the observation time list $\{t^{(i)}_{\text{obs}}\}$ and the flipping time list $\{t^{(i)}_{\text{flip}}\}$ into $\{t^{(i)}_{\text{merge}}\}$. The difference between adjacent elements in $\{t^{(i)}_{\text{flip}}\}$ is distributed according to $Exp[F]$, and is independent among different swimmers, whereas $\{t^{(i)}_{\text{obs}}\}$ is arbitrary and is the same for all swimmers. Here $\{d^{(i)}\}$ is the list for swimming directions according to $\{t^{(i)}_{\text{merge}}\}$

.

1. Generate the initial swimming direction knowing that the probability of following $s_+(x)$ is $\int_0^L P_+(x,0)dx$.

2. Once the initial direction is generated, then draw the initial location from the (re-scaled) quantile function determined by $P_+(x,0)$ or $P_-(x,0)$ accordingly.

The domain mapping functions $y_\pm(x)$, $x_\pm(y)$ and the domain sizes $l_\pm > 0$ are defined as

$$y_+(x) = \int_0^x \frac{1}{s_+(z)}dz, \quad l_+ = y_+(L); \tag{4.2}$$

$$y_-(x) = -\int_L^x \frac{1}{s_-(z)}dz, \quad l_- = y_-(0). \tag{4.3}$$

$x_+(y)$ and $x_-(y)$ are then constructed as the inverse functions of $y_+(x)$ and $y_-(x)$ respectively. The inverse functions are well-defined because $s_\pm(x)$ are single-signed. As a reminder, y_+ and y_- are indeed the system characteristics starting at $x = 0$

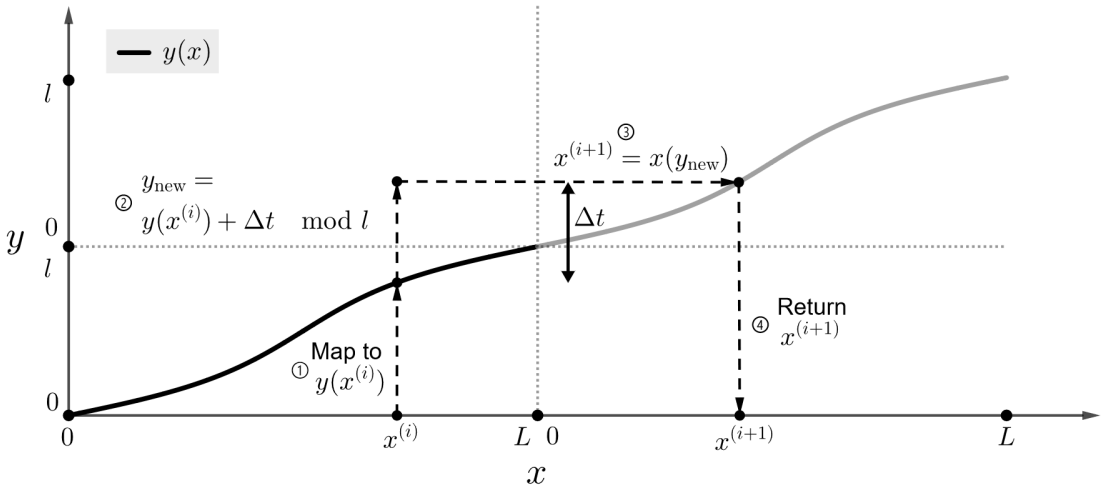

Figure 4.2: Illustration of calculating the new location $x^{(i+1)}$ by domain mapping between x and y in 4 steps. Here, the initial location is $x^{(i)}$, swimming time is Δt, $y = y_{\pm}$ depending on the swimming direction.

.

and L respectively. Using similar techniques, in **Algorithm 2**, the cumulative density function are computed as

$$G_{\pm}(x) = \int_0^x P_{\pm}(z, 0)dz. \tag{4.4}$$

Then we use the same data to construct the quantile functions

$$\begin{cases} Q_+(u) = G_+^{-1}, & u \in [0, G_+(L)], \\ Q_-(u) = G_-^{-1}, & u \in [0, G_-(L)]. \end{cases} \tag{4.5}$$

similarly. The actual code is further vectorized for parallel computation performance.

Interpolation Error Analysis

To speed up the computation, we choose to avoid computing $y_{\pm}(x)$ by integration (4.2, 4.3) and $x_{\pm}(y)$ by definition every time when used for the domain mapping. Instead, we construct the linear interpolated function $y_+^N(x)$ by evaluating $y_+(x)$ from definition (4.2) over N evenly spaced sample points in x, and linearly interpolate its value between two adjacent sample points. Now we use the same data but exchange the

Algorithm 1 Simulation for One Swimmer

Goal: Find the location of a swimmer at each observation time in $\{t_{\text{obs}}^{(i)}\}$.

Require: The initial location $x_{\text{loc}}^{(0)}$ and the initial swimming direction $d^{(0)}$, the speed $s_{\pm}(x)$, the turning rate F, domain size L, the time of observations $\{t_{\text{obs}}^{(i)}\}$ where $t_{\text{obs}}^{(0)} = 0$ and the final time $t_{\text{obs}}^{(n)} = T$, the domain mapping functions $x_{\pm}(y)$ and $y_{\pm}(x)$, the domain size $l_{\pm}$ for $y_{\pm}$.

Construct the flipping time list $\{t_{\text{flip}}^{(i)}\}$ by repeatedly drawing $\Delta t \sim Exp[F]$, where $t_{\text{flip}}^{(i+1)} = t_{\text{flip}}^{(i)} + \Delta t$, until some $t_{\text{flip}}^{(i)}$ surpasses T the final time;

Merge and sort from small to large the observation time list $\{t_{\text{obs}}^{(i)}\}$ with the flipping time list $\{t_{\text{flip}}^{(i)}\}$ into one re-indexed time list $\{t_{\text{merge}}^{(i)}\}$;

Generate a direction list $\{d^{(i)}\}$ that has the same dimension as $\{t_{\text{merge}}^{(i)}\}$, such that $d^{(i)} \in \{1, -1\}$ indicates the swimming direction right after $t_{\text{merge}}^{(i)}$;

Generate a location list $\{x_{\text{loc}}(t_{\text{merge}}^{(i)})\}$ that has the same dimension as $\{t_{\text{merge}}^{(i)}\}$, and initiate $x_{\text{loc}}(t_{\text{merge}}^{(0)}) \leftarrow x_{loc}^{(0)}$;

$i \leftarrow 0$;

while $t_{\text{merge}}^{(i)} \leq T$ **do**

  if $d^{(i)} = 1$ **then**

    Calculate $y_{+}(x_{\text{loc}}(t_{\text{merge}}^{(i)}))$;

    Update $y_{\text{new}} \leftarrow [y_{+}(x_{\text{loc}}(t_{\text{merge}}^{(i)})) + (t_{\text{merge}}^{(i+1)} - t_{\text{merge}}^{(i)})] \mod l_{+}$;

    $x_{\text{loc}}(t_{\text{merge}}^{(i+1)}) \leftarrow x_{+}(y_{\text{new}})$;

  else

    Calculate $y_{-}(x_{\text{loc}}(t_{\text{merge}}^{(i)}))$;

    Update $y_{\text{new}} \leftarrow [y_{-}(x_{\text{loc}}(t_{\text{merge}}^{(i)})) + (t_{\text{merge}}^{(i+1)} - t_{\text{merge}}^{(i)})] \mod l_{-}$;

    $x_{\text{loc}}(t_{\text{merge}}^{(i+1)}) \leftarrow x_{-}(y_{\text{new}})$;

  end if

  $i \leftarrow i + 1$;

end while

Extract the list $\{x_{\text{loc}}(t_{\text{obs}}^{(i)})\}$ from the list $\{x_{\text{loc}}(t_{\text{merge}}^{(i)})\}$;

Return The list $\{x_{\text{loc}}(t_{\text{obs}}^{(i)})\}$;

dependent variable and the independent variable to construct the linear interpolated function $x_+^N(y)$ numerically. $y_-^N(x)$ and $x_-^N(y)$ are constructed similarly but from (4.3).

Nevertheless, using linear interpolated functions speeds up the computation significantly at some cost of accuracy. We now quantify the error introduced through the linear interpolation by looking at individual swimmers: Consider a swimmer whose location is calculated exactly, and another swimmer following the same starting location, initial direction, and the flipping schedule in the same system, except that its location is calculated through the linear interpolated mapping functions. Given $\{t_{\text{obs}}^{(i)}\}$, we aim to estimate an upper bound of the deviation between the two swimmers at the end of a simulation for most of the swimmers, and how fast this error upper bound decreases when we use a finer mesh for the linear interpolation.

To do so, at first we observe from **Algorithm 1** that the interpolation error is only realized when we calculate $y_\pm(x)$ or $x_\pm(y)$ in line 8 and 10, or 12 and 14, i.e., 2 times for each point in $\{t_{\text{merge}}^{(i)}\}$. In one simulation, denote the total number of times for realizing such interpolation errors as n_{e}. Firstly, denote

$$n_{\text{merge}} = \text{number of points in list } \{t_{\text{merge}}^{(i)}\}, \tag{4.6}$$

$$n_{\text{flip}} = \text{number of points in list } \{t_{\text{flip}}^{(i)}\}, \tag{4.7}$$

$$n_{\text{obs}} = \text{number of points in list } \{t_{\text{obs}}^{(i)}\}. \tag{4.8}$$

Then, assuming $\{t_{\text{obs}}^{(i)}\}$ does not overlap with $\{t_{\text{flip}}^{(i)}\}$ (with predetermined list $\{t_{\text{obs}}^{(i)}\}$ they do not overlap almost surely):

$$n_e = 2n_{\text{merge}} = 2(n_{\text{flip}} + n_{\text{obs}}). \tag{4.9}$$

Note that n_e is a random variable, since n_{flip} is Poisson distributed with rate $\lambda = FT$:

$$n_{\text{flip}} \sim \text{Poiss}(FT). \tag{4.10}$$

Further, defining $\bar{n}_e(\alpha)$ as follows:

$$\bar{n}_e(\alpha) = \inf_{N\geq 0}\{N \in \mathbb{Z} : Prob\{n_e \geq N\} < \alpha\}, \quad \alpha \in (0,1). \tag{4.11}$$

For example, if $\alpha = 0.05$, then the random variable n_e falls under $\bar{n}_e(\alpha)$ with probability $1 - \alpha = 0.95$. One can then calculate $\bar{n}_e(\alpha)$:

$$\begin{aligned}\bar{n}_e(\alpha) &= \inf_{N \geq 0}\{N \in \mathbb{Z} : Prob\{n_{\text{flip}} \geq \frac{N}{2} - n_{\text{obs}}\} < \alpha\} \\ &= 2\left(q_{\text{Poiss(FT)}}(1-\alpha) + n_{\text{obs}}\right). \end{aligned} \tag{4.12}$$

Here $q_{\text{Poiss(FT)}} : (0,1) \to \mathbb{Z}$ is the quantile function for a Poisson-distributed random variable with rate FT. It returns the smallest integer n, such that

$$\text{CDF}[\text{Poiss}(FT), n] \geq 1 - \alpha.$$

This quantile function $q_{\text{Poiss(FT)}}$ has no closed-form solution to the best of our knowledge. However, it is available in most standard statistical software packages for numerical evaluation.

We then find the maximum deviation of $y_{\pm}(x)$ from $y_{\pm}^N(x)$:

$$\|y_+ - y_+^N\|_\infty = \max_{0 \leq x \leq L} |y_+(x) - y_+^N(x)|, \tag{4.13}$$

$$\|y_- - y_-^N\|_\infty = \max_{0 \leq x \leq L} |y_-(x) - y_-^N(x)|. \tag{4.14}$$

Consider the case for y_+: within any interval $[x_a, x_b]$ formed by adjacent sampling points x_a and x_b (thus $x_b - x_a = \frac{L}{N-1}$), $y_+(x)$ is only evaluated at the boundary x_a and x_b for the linear interpolation. According to the Interpolation Error Theorem for 2 sample points (Shen, 2019):

$$y_+(x) - y_+^N(x) = \frac{y_+''(x_c)}{2}(x - x_a)(x - x_b), \quad \text{for some} \quad x_c \in (x_a, x_b). \tag{4.15}$$

That is, suppose $|y_+''(x)| \leq 2C_{y_+}$ for some positive constant C_{y_+} for all $x \in [0, L]$, we have

$$\max_{0 \leq x \leq L} |y_+(x) - y_+^N(x)| \leq \frac{1}{2} \max_{0 \leq x \leq L} |y_+''(x)| \left(\frac{L}{N-1}\right)^2 \leq C_{y_+} \left(\frac{L}{N-1}\right)^2 \approx \frac{L^2 C_{y_+}}{N^2} \tag{4.16}$$

Similarly, suppose

$$|y_-''(x)| \leq 2C_{y_-}, \quad x \in [0, L], \tag{4.17}$$

we arrive at

$$\max_{x\in L}|y_-(x)-y_-^N(x)|\leq C_{y_-}\left(\frac{L}{N-1}\right)^2\approx\frac{L^2C_{y_-}}{N^2}. \tag{4.18}$$

For $x_+(y)$, suppose for an arbitrary interval $[x_a,x_b]$ with x_a and x_b being adjacent sampling points, we denote $y_+(x_a)=y_a$, $y_+(x_b)=y_b$. Argued similarly from the Interpolation Error Theorem

$$x_+(y)-x_+^N(y)=\frac{x_+''(y_c)}{2}(y-y_a)(y-y_b),\quad \text{for some}\quad y_c\in(y_a,y_b). \tag{4.19}$$

By the Mean Value Theorem,

$$y_b-y_a=\frac{x_b-x_a}{x_+'(y_d)}\quad \text{for some}\quad y_d\in(y_a,y_b). \tag{4.20}$$

Thus, supposing $\frac{1}{x_+'(y)}\leq C_{x_+,1}$ for some positive constant $C_{x_+,1}$ for all $y\in[0,l_+]$, we have

$$|y-y_a|,|y-y_b|\leq|y_b-y_a|\leq C_{x_+,1}|x_b-x_a|=\frac{LC_{x_+,1}}{N-1}. \tag{4.21}$$

Now suppose $|x_+''(y)|\leq 2C_{x_+},\forall y\in[0,l_+]$, when combined with (4.19, 4.21) it leads to

$$\max_{0\leq y\leq l_+}|x_+(y)-x_+^N(y)|\leq C_{x_+}\left(\frac{LC_{x_+,1}}{N-1}\right)^2\approx\frac{L^2C_{x_+,1}^2C_{x_+}}{N^2}. \tag{4.22}$$

Similarly from the bounds

$$\frac{1}{x_-'(y)}\leq C_{x_-,1},\quad |x_-''(y)|\leq 2C_{x_-},\quad \forall y\in[0,l_-], \tag{4.23}$$

we conclude

$$\max_{0\leq y\leq l_-}|x_-(y)-x_-^N(y)|\leq C_{x_-}\left(\frac{LC_{x_-,1}}{N-1}\right)^2\approx\frac{L^2C_{x_-,1}^2C_{x_-}}{N^2}. \tag{4.24}$$

See Fig. 4.3 for plot of $\|y_\pm-y_\pm^N\|_\infty$ and $\|x_\pm-x_\pm^N\|_\infty$ with respect to N. Denote the maximum of the four as

$$\mathcal{E}_N=\max\{\|x_+-x_+^N\|_\infty,\|x_--x_-^N\|_\infty,\|y_+-y_+^N\|_\infty,\|y_--y_-^N\|_\infty\}, \tag{4.25}$$

and note that by (4.16, 4.18, 4.22, 4.24) we have

$$\mathcal{E}_N\sim O(\frac{1}{N^2}). \tag{4.26}$$

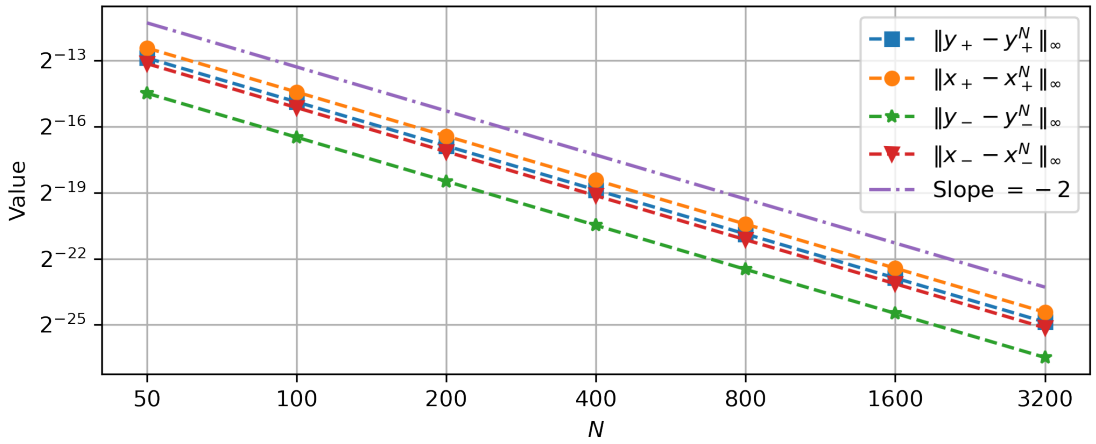

Figure 4.3: Plot of the maximum deviation of $y_\pm(x)$ and $x_\pm(y)$ from their linear interpolated functions $y_\pm^N(x)$ and $x_\pm^N(x)$ respectively, where N is the number of evenly spaced points in x used for interpolation. Here we choose $s_+(x) = \cos(2\pi x) + 2$, $s_-(x) = -\cos(2\pi x) - 3$. We observe that $\|y_+ - y_+^N\|_\infty$, $\|y_- - y_-^N\|_\infty$, $\|x_+ - x_+^N\|_\infty$ and $\|x_- - x_-^N\|_\infty$ all decrease at $O(\frac{1}{N^2})$, as expected.

Therefore, the total error introduced by the linear interpolation for one swimmer is estimated at most

$$n_e \mathcal{E}_N \sim n_e O(\frac{1}{N^2}). \tag{4.27}$$

We can further conclude that with probability $(1 - \alpha)$, the total error from linear interpolated mapping functions for a swimmer is estimated at most

$$\bar{n}_e(\alpha)\mathcal{E}_N \sim \bar{n}_e(\alpha) O(\frac{1}{N^2}). \tag{4.28}$$

For an example such as the Monte-Carlo simulation in Fig. 3.2, we use $N = 10001$, $T = 10$, $F = 1$, $s_+(x) = \cos(2\pi x)+1.5 = -s_-(x)$. In this case, it can be calculated from (4.12) that $\bar{n}_e(0.0014) \approx 2000$, and $\mathcal{E}_{10001} \approx 9.8 \times 10^{-9}$. Therefore, with probability of 0.9986, the total error introduced by linear interpolation for one swimmer is at most

$$\bar{n}_e(0.0014)\mathcal{E}_{10001} \approx 1.96 \times 10^{-5}.$$

Thus, the interpolation error introduced in this case is small.

Algorithm 2 Generate Initial Direction and Location

Goal: Find the random initial location $x_{\text{loc}}^{(0)}$ and direction $d^{(0)}$ of a swimmer according to the initial distribution $P_{\pm}(x, 0)$.

Require: The probability of moving to left or right $G_{\pm}(L)$, the quantile function $Q_{\pm}(u)$.

Draw $u_1 \sim Unif(0, 1)$;
if $u_1 \leq G_+(L)$ **then**
    $d^{(0)} \leftarrow 1$;
else
    $d^{(0)} \leftarrow -1$;
end if
Draw $u_2 \sim Unif(0, 1)$;
if $d^{(0)} = 1$ **then** $Q_+(u) = G_+^{-1}$;
    $x_{\text{loc}}^{(0)} \leftarrow Q_+(u_2 G_+(L))$;
else
    $x_{\text{loc}}^{(0)} \leftarrow Q_-(u_2 G_-(L))$;
end if
Return The initial location $x_{\text{loc}}^{(0)}$ and direction $d^{(0)}$;

4.1.3 Computational Challenges when $s_+(x)$ Has a Root

Notice that this Monte-Carlo algorithm relies on the bijective mapping between the physical location x and the time domain variable $y_{\pm}$: $y_{\pm}(x)$ is the time taken to swim from 0 to x in the given swimming direction according to speed $s_{\pm}(x)$ respectively. However, there is no bijective mapping between x and y_+ if $s_+(x)$ has roots.

For example, take $s_+(x) = \cos(2\pi x)$ with the sink root at $x_1 = \frac{1}{4}$ and the source root at $x_3 = \frac{3}{4}$. Fix $y_+(0) = 0$, then $y_+(x)$ for $x \in [x_1, 1]$ becomes undefined, because the swimmer cannot move across x_1 by following $s_+(x)$. As a result, we cannot calculate the swimming time using **Algorithm 1**.

One may suggest conducting the Monte-Carlo simulation by following the characteristic curves of $P_{\pm}$, since the swimmer does not change its direction in the time interval between adjacent elements in $\{t_{\text{merge}}^{(i)}\}$. A characteristic curve $t(x)$ can be solved from the ODE

$$\frac{dt}{dx} = \frac{1}{s(x) - 1} \tag{4.29}$$

with an initial condition.

There are at least two issues one may encounter when adopting this approach: Sensitivity to initial distributions, and difficulty in calculating the characteristic curve accurately. The sensitivity issue comes from that the characteristics starting close to the source can diverge quickly, and the swimmers near the source following the diverging characteristics may end up far apart, albeit in finite distance. Thus the final locations are relatively sensitive to the initial distribution of $P_{\pm}$. See Fig. 3.7 for an example: varying the initial location near x_3 by just 0.0002 we get drastically different characteristic curves. Note that the sensitivity to initial conditions can be alleviated by using more agents in the simulation, and this issue is less significant when compared to the following accuracy issue in our experiment. The accuracy issue arises from the practical side: For a starting point near the roots x_1 or x_3, where $\frac{1}{s-1}$ is close to singularity, accurately integrating $\frac{1}{s-1}$ to get the characteristic curve can be challenging and its performance depends heavily on the integration algorithm, especially when $s(x)$ does not have a closed form expression.

We also conduct a controlled experiment where $s(x)$ is piecewise linear, so that the characteristic curves can be calculated exactly, thus eliminating the accuracy issue. We compare this Monte-Carlo result with the model used in Fig. 3.2, where there is no roots for s_+ and the domain mapping method is employed. See Fig. 4.4 for the plot.

Therefore, given that usually only a small portion of the swimmers appear near x_3 in our simulation at any given time, and we generally use a large number of agents for running the Monte-Carlo, this sensitivity issue is not a major problem from our observations. However, in general it is quite difficult to calculate the characteristics accurately in a Monte-Carlo using arbitrary $s(x)$. In our case where $s(x) = s(c(x))$ and $c(x)$ being a series solution from (2.17), it is especially so. As a result, we use a finite difference method instead of a Monte-Carlo algorithm to validate our analytical solution when the relative speed has roots.

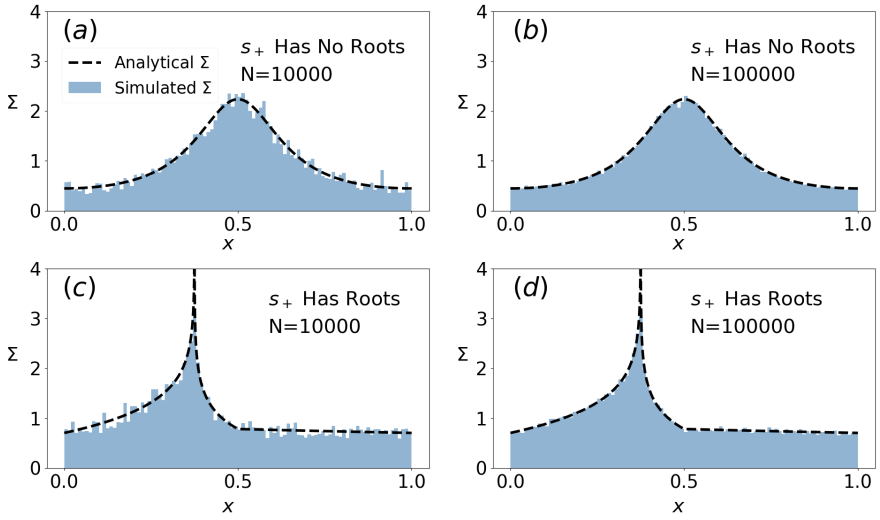

Figure 4.4: The blue histograms represent the results from agent-based Monte-Carlo experiments terminated at large time to approximate the steady state, and the black dashed lines stand for the corresponding analytical solutions at steady state. For plot (a) and (b), $s_+(x) = s_-(x) = \cos(2\pi x) + 1.5$. For plot (c) and (d), $s_+ = s - 1$, $s_- = s + 1$ with $s(x) = (-(x - x_1) + 1)\mathbb{1}_{0\le x\le 0.5} + ((x - x_3) + 1)\mathbb{1}_{0.5<x\le 1}$, where $\mathbb{1}$ is the indicator function, $x_1 = 0.375$, $x_3 = 0.625$. s is chosen to be piecewise linear to calculate the characteristics accurately for this experiment. We observe that both Monte-Carlo schemes can converge to the analytical solution provided enough agents, and therefore the diverging characteristics near the source do not impose too much sensitivity issue, provided that accuracy is not a concern.

4.2 Finite Difference Scheme

To select an appropriate finite difference scheme for solving (4.1), we note that the swimming direction changes across x_1 and x_3. Moreover, the Frobenius analysis indicates a possible blow-up (discontinuity) at the sink, while always having a smooth solution at the source. To take those into account, we adopt techniques for handling flux direction changes and producing smooth solutions for rarefaction waves in building our finite difference scheme. In comparison, characteristic curves of P_- are well-behaved (See Fig. 3.8 for an example.): $\frac{dt}{dx} = \frac{1}{s_-(x)}$ is bounded, and P_- is known to have a bounded and continuous analytical solution. Thus we expect its finite difference scheme to be relatively simple to build. Therefore, we focus our discussion on building a scheme for calculating P_+.

We base our numerical scheme on the first order upwind scheme for the following reasons: The solutions of $P_{\pm}(x)$ depend heavily on $s_{\pm}(x)$. Given that $s_{\pm}(x)$ are arbitrary, $P_{\pm}$ are not necessarily smooth, especially when we have a blow-up. In this case, higher order methods tend to introduce large non-physical oscillations in our experiments near the blow-up, and sometimes result in an unstable scheme. For example, in Fig. 4.5, the Richtmyer two-step Lax–Wendroff method with explicit source terms tends to have oscillations for small value of F and for large value of $|s'(x_1)|$, whereas in some cases it does produce an answer consistent with our analytical result. For this reason, we decide not to use this Richtmyer two-step Lax–Wendroff scheme. As a result, we want to limit ourselves to monotone and total variation diminishing (TVD) schemes to produce a physical solution. Therefore, we use only first order methods. We are aware that the Lax-Friedrichs scheme can naturally handle two different flux directions of P_+ and is quite robust, however it introduces too much viscosity, and does not produce an expected blow-up at x_1 even when the analytical result suggests so. See Fig. 4.6 for an example. In the end, we choose the simple and robust first order upwind scheme with necessary adaptations discussed below. See Fig. 4.8 for its performance.

Note that in our case the flux direction of P_+ is different inside and outside of (x_1, x_3). For the ease of discussion, rewrite the fluxes in (4.1) as

$$\begin{cases} M_+(x,t) = s_+(x)P_+(x,t) \\ M_-(x,t) = -s_-(x)P_-(x,t). \end{cases} \tag{4.30}$$

Further, we impose that x_1, x_3 not on our spatial grid to avoid conducting finite differences directly on the singularities. Indeed, the two grid points closest to x_1, x_3 are special and the following (4.31, 4.32) do not apply. Fig. 4.7 represents the schematic diagram of calculating P_+ without including the source term $F(P_- - P_+)$.

For a grid point $x \in (0, x_1) \cup (x_3, L)$, the flux direction for P_+ is to the right,

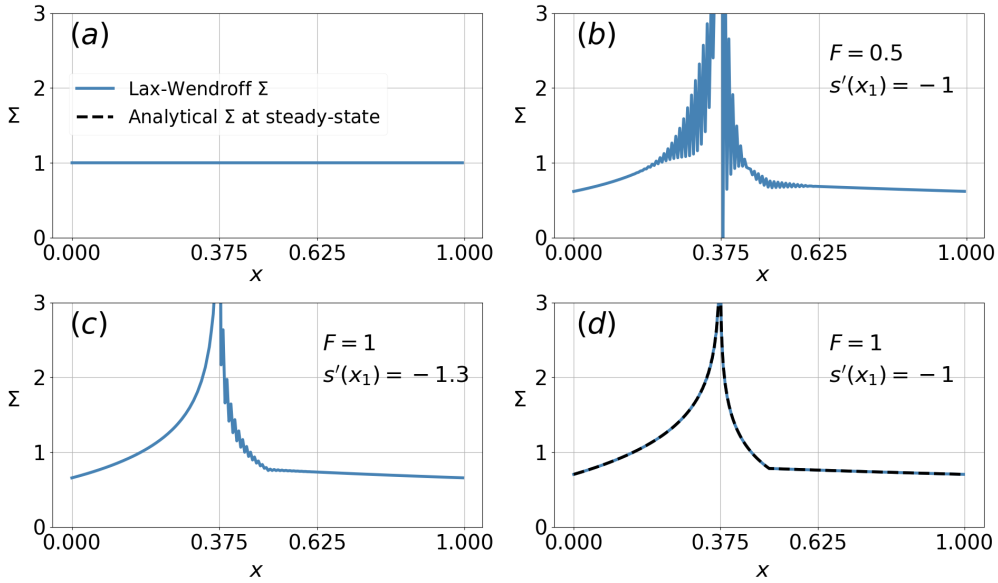

Figure 4.5: The numerical solutions of $\Sigma = P_+ + P_-$ come from the Richtmyer two-step Lax–Wendroff scheme, for 3 systems with different F and different piecewise linear $s(x)$. Let $\beta = |s'(x_1)|$, $x_1 = 0.375$, $x_3 = 0.625$. Specifically, $s(x) = (-\beta(x - x_1) + 1)\mathbb{1}_{0\le x\le 0.5} + (\beta(x - x_3) + 1)\mathbb{1}_{0.5<x\le 1}$, where $\mathbb{1}$ is the indicator function. This scheme tends to have non-physical oscillations for small value of F and large value of $|s'(x_1)|$. Plot (a) is the common initial condition for the 3 systems such that $P_\pm(x, 0) = 0.5$. All 3 systems are terminated at $t = 10$ to approximate the equilibrium. Plot (b) has $s'(x_1) = -1$, $F = 0.5$. Plot (c) has $s'(x_1) = -1.3$, $F = 1$. Both (b) and (c) render non-physical oscillations. Plot (d) has $s'(x_1) = -1$, $F = 1$ and produces a result consistent with the analytical solution.

therefore the upwind scheme is

$$\begin{aligned} P_+(x, t + \Delta t) = P_+(x, t) - \frac{\Delta t}{\Delta x}\left[M_+(x, t) - M_+(x - \Delta x, t)\right] \\ + F\left[P_-(x, t) - P_+(x, t)\right]\Delta t. \end{aligned} \tag{4.31}$$

Similarly, for a grid point $x \in (x_1, x_3)$ the flux direction for P_+ is to the left and thus the upwind scheme is

$$\begin{aligned} P_+(x, t + \Delta t) = P_+(x, t) - \frac{\Delta t}{\Delta x}\left[M_+(x + \Delta x, t) - M_+(x, t)\right] \\ + F\left[P_-(x, t) - P_+(x, t)\right]\Delta t. \end{aligned} \tag{4.32}$$

Denote the two grid points, $x_{1,l}$ and $x_{1,r}$, closest to x_1 from the left and the side respectively. The flux for P_+ at x_1 must be 0 at all time following (4.30): $s_+(x)$ has a

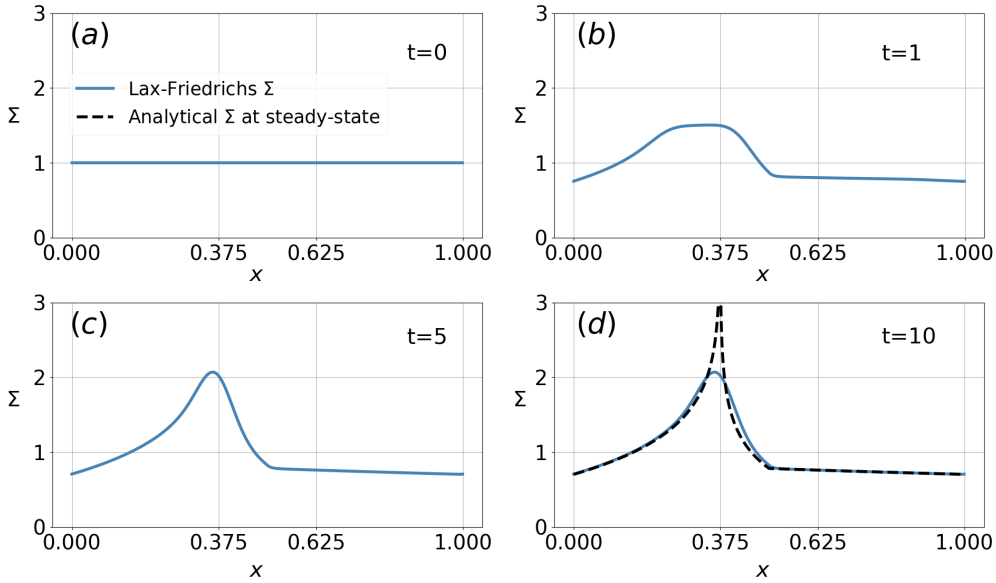

Figure 4.6: The numerical solution of $\Sigma = P_+ + P_-$ coming from the Lax-Friedrichs scheme. Here $s(x)$ is (4.40) and we expect an integrable singularity for Σ at $x_1 = 0.375$ at the steady-state . The Lax-Friedrichs scheme introduces too much viscosity that smooths out the blow-up.

simple root at x_1 and P_+ has at worst an integrable singularity. Therefore in the finite difference scheme, we approximate this zero-flux condition by imposing the flux M_+ to be 0 at $x_{1,l}$ and $x_{1,r}$:

$$M_+(x_{1,l}, t) = 0 = M_+(x_{1,r}, t). \tag{4.33}$$

Following the upwind principle we arrive at

$$\begin{aligned} P_+(x_{1,l}, t + \Delta t) = P_+(x_{1,l}, t) - \frac{\Delta t}{\Delta x} \left[0 - M_+(x_{1,l} - \Delta x, t)\right] \\ + F\left[P_-(x_{1,l}, t) - P_+(x_{1,l}, t)\right] \Delta t; \end{aligned} \tag{4.34}$$

$$\begin{aligned} P_+(x_{1,r}, t + \Delta t) = P_+(x_{1,r}, t) - \frac{\Delta t}{\Delta x} \left[M_+(x_{1,r} + \Delta x, t) - 0\right] \\ + F\left[P_-(x_{1,r}, t) - P_+(x_{1,r}, t)\right] \Delta t. \end{aligned} \tag{4.35}$$

At the grid point x closest to x_3, the Frobenius analysis suggests a smooth

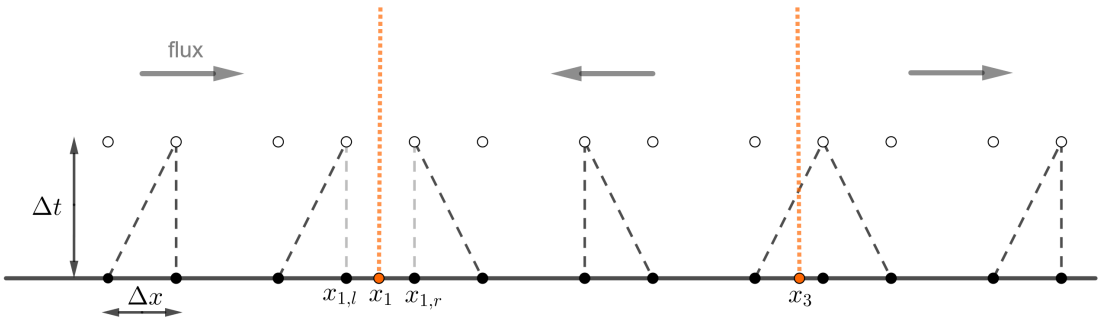

Figure 4.7: Schematic diagram of the finite difference scheme described in (4.31 - 4.36) to calculate P_+. The fluxes at $x_{1,l}$ and $x_{1,r}$ are set to be 0, hence the lighter shade of gray. Here we did not include the source term $F(P_- - P_+)$ for a clearer view.

solution for P_+ near x_3, hence we introduce numerical viscosity by using the Lax-Friedrichs scheme

$$\begin{aligned} P_+(x,t+\Delta t) = P_+(x,t) &- \frac{\Delta t}{2\Delta x}\left[M_+(x+\Delta x,t) - M_+(x-\Delta t,t)\right] \\ &+ \frac{1}{2}[P_+(x+\Delta x,t) - 2P_+(x,t) + P_+(x-\Delta x,t)] \\ &+ F\left[P_-(x,t) - P_+(x,t)\right]\Delta t. \end{aligned} \tag{4.36}$$

For P_-, the flux direction is always the left, and the upwind scheme is straight forward:

$$\begin{aligned} P_-(x,t+\Delta t) = P_-(x,t) &- \frac{\Delta t}{\Delta x}\left[M_-(x+\Delta x,t) - M_-(x,t)\right] \\ &+ F\left[P_+(x,t) - P_-(x,t)\right]\Delta t. \end{aligned} \tag{4.37}$$

Here, suppose

$$c = \max\{\max_x |s_+(x)|, \max_x |s_-(x)|\} \tag{4.38}$$

is the global maximum of swimming speeds for both directions, and we need to choose Δx and Δt accordingly so that the Courant-Friedrichs-Lewy (CFL) condition

$$\frac{c\Delta t}{\Delta x} \leq 1 \tag{4.39}$$

is satisfied.

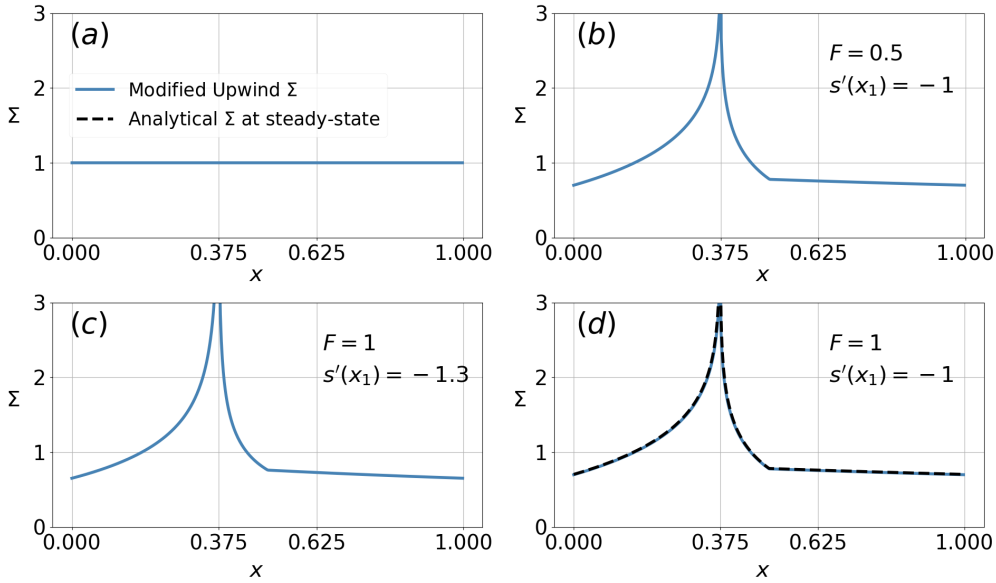

Figure 4.8: The numerical solutions of $\Sigma = P_+ + P_-$ come from our modified upwind scheme, for 3 systems with different F and different piecewise linear $s(x)$. The settings are identical to that of Fig. 4.5. This modified upwind scheme does not have non-physical oscillations for all cases considered here when compared to the Richtmyer two step Lax-Wendroff scheme, and does not introduce too much viscosity to damp the blow-up when compared to the Lax-Friedrichs scheme. Note that we only have the closed-form analytical solution for setting (d) available.

4.3 Results

In this section, we compare the analytical solutions against our numerical results for validation.

4.3.1 $s - 1$ Has No Roots

4.3.1.1 $s(x) > 1, x \in [0, 1]$

We plot the steady-state analytical solution together with an agent-based Monte-Carlo simulation in Fig. 4.9 for an example: here we used an $s(c)$ that is a linear function of c for demonstration, i.e., a higher toxin concentration linearly corresponds to a lower speed. We observe that the maximum of prey's density is achieved where the toxin has the highest concentration, the position of the Karlodinium.

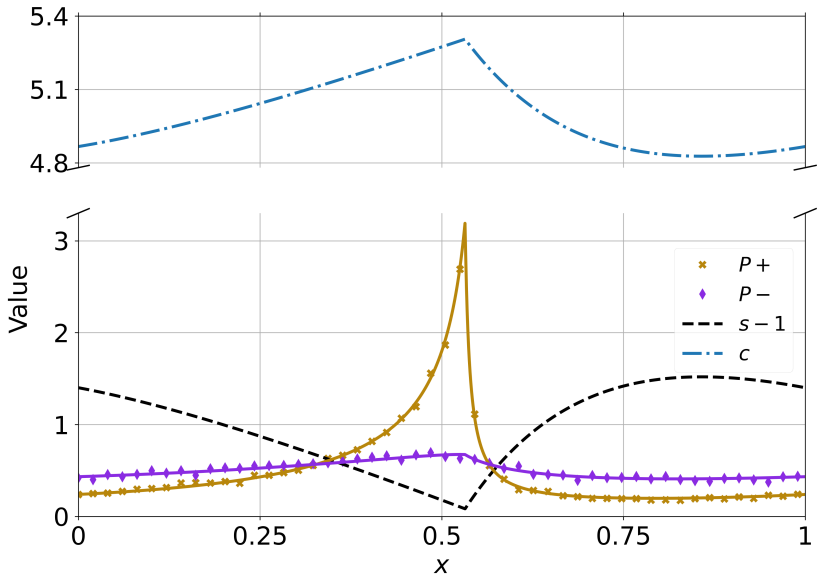

Figure 4.9: Points represent the result from a Monte-Carlo simulation of the system (3.15) after it relaxes to being stationary. Lines represent its corresponding analytical solution. Here c is calculated from (2.17) with $\gamma = 0.532154$, $\beta = 0.2$, $\kappa = 0.2$ and $s = -3c + 17$. Note that $s(x)$ reaches its minimum at γ, leading to the maximum density for both P_+ and P_-.

4.3.1.2 $s(x) < 1, x \in [0, 1]$

Although the process in finding its analytical solution is identical to the case when $s(x) > 1$, the result is quite different. See Fig. 4.10 for an example where we still use $s(c)$ that is linear with c, but with different coefficients so that $0 < s(x) < 1$. Note that prey's density Σ stays relatively flat due to the constraint of $s(x)$ and there is no clear aggregation when $s < 1$.

4.3.2 $s - 1$ Has Roots

4.3.2.1 $s'(x_1) \leq -1$

In this case, P_+ has an integrable singularity at x_1. First we present the convergence study by comparing the steady-state analytical solution (3.94-3.97) with its

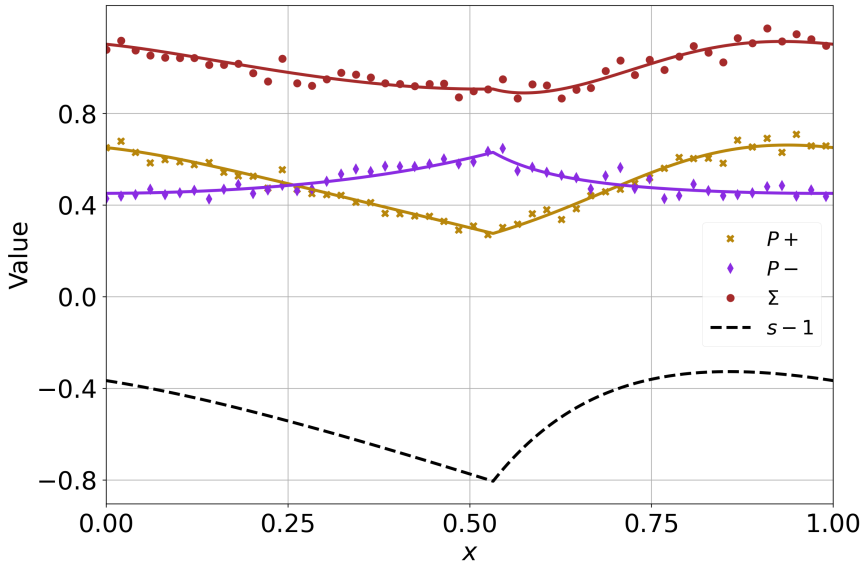

Figure 4.10: Points represent the solutions from a Monte-Carlo simulation of the system (3.15) after it relaxes to being stationary. Lines represent its corresponding analytical solution. Here c is calculated from (2.17) with $\gamma = 0.532154$, $\beta = 0.2$, $\kappa = 0.2$ and $s = -c + 5.5$.

large-time numerical solution using a finite difference scheme, assuming $s(x)$ is piecewise linear. $s(x)$ is chosen to be piecewise linear here since $\mu(x)$ in this case has a closed-form expression that can be evaluated exactly. Specifically, we choose:

$$s(x) = \begin{cases} -x + \frac{9}{8}, & x \in [0, \frac{1}{2}], \\ x + \frac{1}{8}, & x \in (\frac{1}{2}, 1]. \end{cases} \tag{4.40}$$

We plot in Fig. 4.11 the number of mesh points against the error in η calculated from (3.74) in the log-log scale to validate our numerical scheme.

We then plot in Fig. 4.12 the numerical solution for $s(x)$ derived from the toxin concentration discussed in (2.17), with $s(c) = -3c + 16$. Note that in this case, the location of the maximum in prey density does not coincide with the location of the maximum toxin concentration ($x \simeq 0.532$ on the plot). Instead, the spike occurs at x_1, the location of the sink. It is also a global maximum for Σ. Also, near the source x_3, $P_\pm$ stays regular at steady-state.

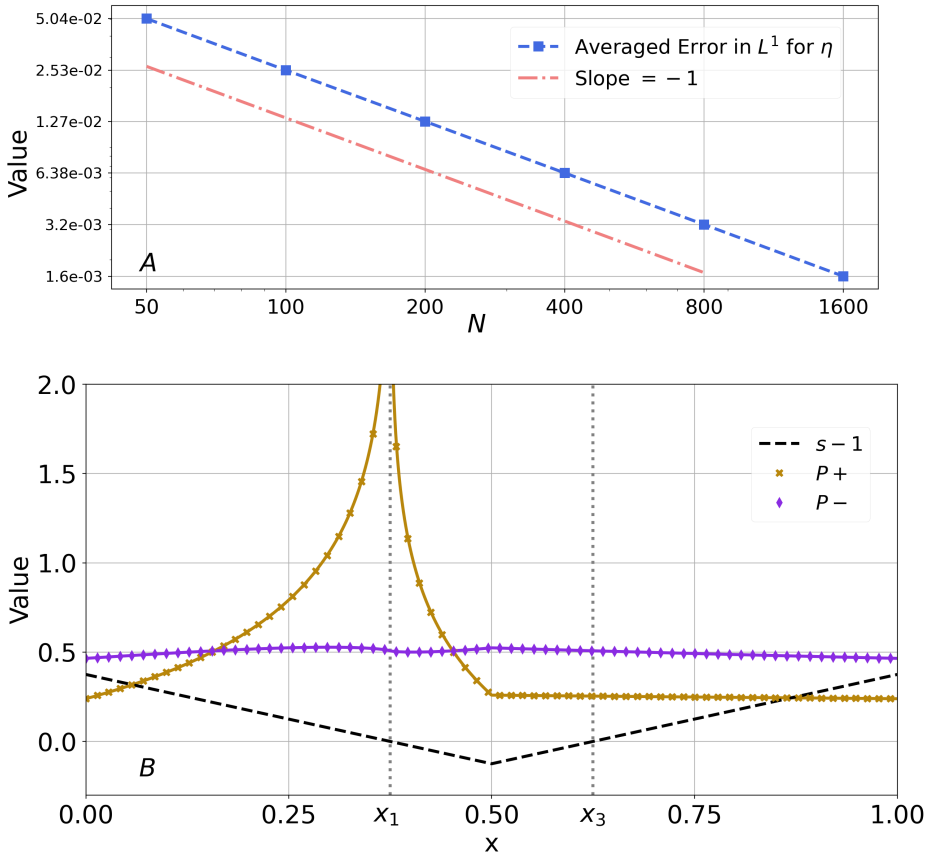

Figure 4.11: Plot A is the log-log plot for the averaged error in L^1 norm, i.e., $\frac{1}{N}\sum_{n=0}^{N}|\eta_{\text{num}}(n) - \eta^*|$, where $\eta_{\text{num}}(n)$ is the numerical value for η at the n-th mesh point, $\eta^* \simeq -0.98384$ is the analytical value, and N is the number of mesh points. It shows that our upwind scheme converges at $O(\Delta x)$, where $\Delta x = \frac{1}{N-1}$ is the mesh size. In plot B, the discrete points are from the finite difference scheme at a large time to approximate the equilibrium, and the solid lines are analytical solutions from (3.94-3.97). Here s is the piecewise linear function described in (4.40)

4.3.2.2 $-1 < s'(x_1) < 0$

We construct $s(x) = -c(x) + 6$ such that $s'(x_1) \simeq -0.805$ in Fig. 4.13. From the Frobenius analysis, the leading orders terms of $P_+ = O(1) + O(|x - x_1|^{0.242})$ for $x \simeq x_1$. Hence P_+ is finite at x_1. It is not differentiable at x_1 but it does have a local maximum there. Again, near x_3, $P_\pm$ stays regular at steady-state. See Fig. 4.13 for its plot.

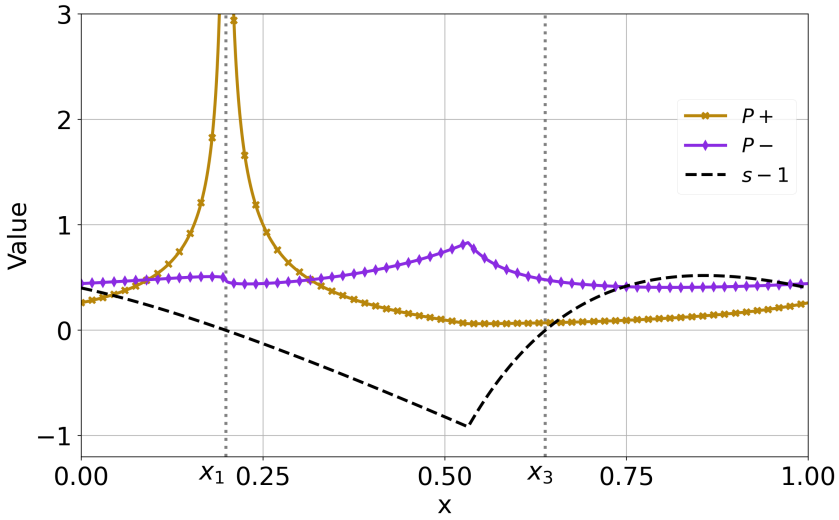

Figure 4.12: The discrete points are generated from the finite difference scheme on (3.15) at a large time to approximate the equilibrium. Solid lines are just connecting the discrete points. Here c is the same from Fig. 4.9 but $s = -3c + 16$ in order for $s - 1$ to generate two roots. $s'(x_1) \simeq -2.41556$, leading to an integrable singularity for P_+.

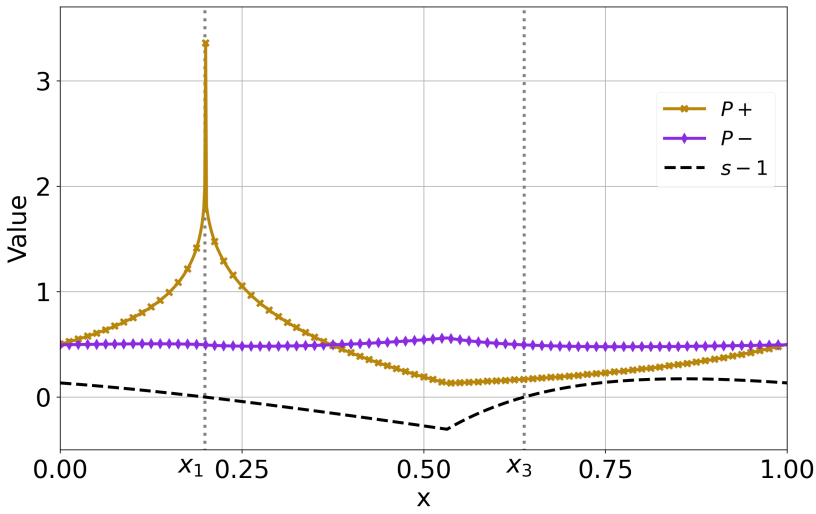

Figure 4.13: The discrete points are generated from the finite difference scheme on (3.15) at a large time to approximate the equilibrium. Solid lines are just connecting the discrete points. Here $s'(x_1) \simeq -0.80518$. In this case, $\nu(x_1) - 1 \simeq 0.24195 > 0$, P_+ does not have the integrable singularity and is therefore finite at x_1.

Summary of Results

In summary, for all cases of $s \pm (x)$ that we consider, the analytical methods we proposed in finding the steady-state distribution of the prey yield consistent results with data from the numerical schemes. Specifically, we see examples of the Monte-Carlo scheme we proposed in Sec. 4.1 working for single-signed $s_{\pm}(x)$. Also, we numerically verified the first order convergence of the finite difference scheme we proposed in Sec. 4.2.

We also directly observe from the plots that the type of aggregation (or no aggregation at all) from prey depends heavily on the exact form of $s_{\pm}(x)$: When $s_{+}(x) > 0$, the prey aggregates around the predator; When $s_{+}(x) < 0$, there is not much aggregation; When $s_{+}(x)$ has two roots where x_1 is the sink root and x_3 is the source root, the plots verify the existence of aggregation near x_1. Specifically, the numerical scheme verifies the conclusion from the Frobenius analysis that if $s'_{+}(x) \leq -1$ then there is an integrable singularity at x_1; if $-1 < s'_{+}(x) < 0$ and $\frac{1}{s'_{+}(x)} \notin \mathbb{Z}$ then there is only a local maximum of the prey density at x_1. Moreover, the numerical result verifies that at x_3, the steady-state density $P_{\pm}$ is always finite, as suggested by the Frobenius analysis.

Chapter 5

CONCLUSION

In this thesis, we have examined in 1-D how prey plankton can form aggregations under the influence of Karlotoxin, a compound secreted by their predator Karlodinium that slows down the prey's swimming speed. Specifically, we studied the density of prey under the generalized Goldstein-Kac framework, where the prey swims in a run-and-tumble fashion with varying speed, and the run time between adjacent tumbles (direction changes) is drawn independently from an exponential distribution. Further, we assume that the toxin does not influence the tumbling.

In this final chapter, we at first summarize the analysis results from our model and relate them to their biological impact. Then we dive into the analytical and numerical methodologies that we implement, and the insights they provide for understanding the model. We specifically mention their contributions to generalizing or expanding existing research. We end the chapter by discussing future research directions under this topic.

For the analysis of the model, we start by examining the case when the toxin concentration is stationary, representing the case when the Karlodinium's location is fixed and the Karlotoxin level has reached its steady-state. For this case, we are able to fully solve for the density of prey at any given time analytically. At steady-state, the prey aggregate at the location where they swim the slowest due to the high concentration of toxin, regardless of the initial conditions. We conclude that Karlotoxin passively emitted from a stationary predator leads to prey aggregation.

Then we suppose that the Karlodinium swims in one direction with constant speed. We start by finding the steady-state distribution of the toxin concentration in

a translating reference frame. We analytically find the steady-state density of the prey under the steady-state toxin field. Here, the relative speed between the predator and the prey characterizes the model: Whether the relative speed has roots or not leads to different system dynamics, as discussed below.

When the prey speed is strictly faster than the predator (i.e., $s - 1 > 0$), aggregation occurs at the place that minimizes the relative speed. It is the place where the Karlotoxin has the highest concentration, which is the location of the predator. When the prey speed is strictly slower than the predator (i.e., $s - 1 < 0$), there is no clear sign of aggregation. Such results suggest that the Karlotoxin slows down and accumulates fast-moving prey, but does not have much effect in aggregation if the prey is already swimming slower than the predator. This is in agreement with the previous case's conclusion when the predator is assumed stationary: The prey always swim no slower than the predator since the predator speed is 0, and we demonstrated the presence of aggregation.

When their relative speed has roots, assuming a sink-type root at x_1 and a source-type root at x_3, there is always aggregation at the sink root but not at the source root. Moreover, the prey's density at the sink can become an integrable singularity, leading to a population blow-up when the relative speed's slope at the sink is steep enough: $s'(x_1) \leq -1$. Note in this case the maximum density of prey is not achieved at the predator's location but at the sink. With the presence of sink and source roots, we see that the location of the prey aggregation depends not only on the prey's response to the toxin, but also on the bio-locomotion of the predator. Overall, depending on the exact shape of $s(x)$ as influenced by the Karlotoxin, the maximum density of prey can occur at the location of the predator or in the wake of the predator's motion.

In the procedure of forming our analytical solutions, we heavily utilize techniques for analyzing linear hyperbolic systems. In the case of having a stationary toxin concentration, we generalize the original Goldstein-Kac system with constant movement speed to having an arbitrary movement speed $s(x)$. The solution is achieved by

mapping from the spatial domain in x to another domain in y with units of time. Physically y is the time to swim from 0 to x under no direction switches. We showed that the domain mapping is in effect calculating the system's characteristic curve starting at $x = 0$. This mapping technique has been used in previous works for analysis or conducting agent-based simulations (Kaplan et al., 1964; Angelani and Garra, 2019), but the physical interpretation of y and its connection with the system characteristics were not formulated to the best of our knowledge.

The Goldstein-Kac system is commonly written in its telegraph equation form for finding analytical solutions (Kaplan et al., 1964; Kac, 1974; Hillen, 2002). However, in existing work, this interpretation was mostly limited to the original Goldstein-Kac system with a constant or piece-wise constant speed. By representing the extended system in its flux form $M_{\pm}(y, t)$, instead of in its density form $P_{\pm}(x, t)$, we are able to transform the system into the telegraph equation and solve it using Fourier series. We also note here that this technique is not limited to only periodic boundary conditions, and in general should be considered a valid approach when the system has identical traveling speeds in both directions.

We also examined the system from the perspective of its characteristic curves. A swimmer follows a characteristic curve $t(x)$ in its run phase, and can instantaneously switch to another characteristic curve when it tumbles to its next run phase. Although the characteristic curves for P_+ we observe bundle near x_1, we should not conclude just from the characteristics that all swimmers following s_+ will aggregate near x_1 eventually, due to not taking direction switches into account. We could also formulate a general agent-based Monte-Carlo for the extended Goldstein-Kac system based on the characteristics. This interpretation allows us to understand when the agent-based Monte-Carlo would not perform well: For example, the presence of a source root makes following an exact characteristic curve starting near the source root an ill-posed problem, because the characteristics originate closely to the source diverge quickly, making the simulation highly sensitive to the initial distributions of $P_{\pm}$. Since our model does come from a rather simple physical system, the poor performance of the agent-based

simulator indicates the system in this case may be modeled differently. We leave the examination of other models to future work.

Under the presence of roots from the relative speed, the system is no longer strictly hyperbolic. Since most analysis work for hyperbolic systems assumed no roots in $\Lambda(x)$ in their characteristic forms (3.17), our tools for finding the steady-state solution are limited. In this case, we choose to conduct a local analysis using the method of Frobenius at the sink root and source root to provide necessary clues on forming the analytical solution, especially when the Monte-Carlo simulation does not work. Specifically, we found a possible blow-up at the sink, while the source always has a smooth solution. Though the method of Frobenius is a commonly used technique for analysing ODEs, its usage was often limited to the simple case where $\sigma_1 - \sigma_2$, the difference of the two indicial roots, is not an integer. We instead have examined in detail when $\sigma_1 - \sigma_2 \in \mathbb{Z}$, and list the iterative formulas for calculating the coefficients in the Frobenius solution. From the method of Frobenius, the analytical steady-state solution (3.94-3.97) of the system covers all cases within our modeling assumptions, including when $\sigma_1 - \sigma_2 \in \mathbb{Z}$; Further, one can compute in a case-by-case basis to investigate whether there is a blow-up under a smooth $s(x)$. We are aware that the method of Frobenius limits our analysis to systems with smooth $s(x)$, and we would like to see local analysis methods that are suitable for more generic choices of $s(x)$.

For the numerical methods for validating our analytical solutions, we prioritize the agent-based Monte-Carlo because it directly simulates the physical system we are modeling. This Monte-Carlo scheme introduces no temporal discretization errors and therefore produces much more accurate locations at the agent level. Also, we use domain mapping for the Monte-Carlo to effectively avoid repeatedly calculating the characteristics during each calculation of location, greatly speeding up the computation. However, when the system introduces singularities, the Monte-Carlo method becomes highly sensitive to initial conditions of $P_{\pm}$, and we switch to finite difference methods for verification as a result. Because finite difference is based on the model PDEs, it is not directly influenced by this agent-level ill-posedness, though the scheme

needs to be adapted accordingly to handle the singularities. We propose a modified first order upwind scheme with necessary adaptations to handle the change of swimming directions near the sink, and the diverging characteristics near the source for P_+. It is a robust scheme that can handle all situations within our modeling framework, and it is tested to be numerically consistent with a known steady-state analytical solution. In our experiment, we find that a second order scheme, the Richtmyer two-step Lax-Wendroff method, only works in some cases, and otherwise produces non-physical oscillations. It will be a worthwhile future investigation to find a higher order finite difference scheme that can generally solve the extended Goldstein-Kac system with or without singularities. For the computation time, to get approximately the same level of accuracy, the finite difference approach is in general faster than the Monte-Carlo. Although by taking advantage of parallel computations in Python and using vectorization, the Monte-Carlo can be sped up significantly.

For future works, apart from the previously mentioned cases, a natural direction is to further analyze the Goldstein-Kac system under different or more general conditions. One can work on quantifying the procedure of forming an aggregation (or a blow-up whenever present) in the extended Goldstein-Kac system, since we currently limit mostly to the steady-state. For instance, estimating the time in forming effective aggregations where the density is above a threshold. Also, how the system behaves under different boundary conditions is worth the investigation and several meaningful cases have already been studied by Angelani and Garra (2019). Moreover, we can assume that the swimming speed also takes influence from the toxin's chemical gradient, and study the system analytically or numerically under chemotaxis as well. Another direction is to introduce the predator-prey population dynamics that is observed realistically: The prey can be consumed, and both the predator and prey reproduce based mostly on their nutrient level. In a 2-D or 3-D setting, this could allow us to further investigate the conditions for population blow-up of the Karlodinium, and could lead to developing applicable preventive measures to control their harmful algae blooms. Going beyond 1-D typically requires different modeling techniques, and we expect to see

heavy use of numerical methods especially Monte-Carlo. Overall, there are still many open problems in the predator-prey population dynamics to study in 2-D and 3-D. Tackling them will not only advance the quantitative understanding of the population dynamics, but also create new tools and insights for conducting stochastic modeling in general.

Bibliography

Anderson, W. J. (2012). *Continuous-time Markov chains: an applications-oriented approach*. Springer Science & Business Media.

Angelani, L. and Garra, R. (2019). Run-and-tumble motion in one dimension with space-dependent speed. *Physical Review E*, 100(5):052147.

Bastin, G. and Coron, J.-M. (2016). *Stability and boundary stabilization of 1-D hyperbolic systems*, volume 88. Springer.

Berg, H. C. (2008). *E. coli in motion*. Springer Science & Business Media.

Berg, H. C. and Brown, D. A. (1972). Chemotaxis in Escherichia coli analysed by three-dimensional tracking. *Nature*, 239(5374):500–504.

Broadwell, J. E. (1964). Shock structure in a simple discrete velocity gas. *The Physics of Fluids*, 7(8):1243–1247.

Cerino, F. and Zingone, A. (2006). A survey of cryptomonad diversity and seasonality at a coastal Mediterranean site. *European Journal of Phycology*, 41(4):363–378.

Childs, P. and Keener, J. (2018). Stochastic switching dynamics of flagellar rotary motors. *Journal of Physics A: Mathematical and Theoretical*, 51(42):425601.

Christlieb, A. J., Rossmanith, J. A., Smereka, P., et al. (2004). The Broadwell model in a thin channel. *Communications in Mathematical Sciences*, 2(3):443–476.

Colton, D. (2004). *Partial differential equations: an introduction*. Courier Corporation.

Cormen, T. H., Leiserson, C. E., Rivest, R. L., and Stein, C. (2009). *Introduction to algorithms*. MIT Press.

Courant, R., Friedrichs, K., and Lewy, H. (1967). On the partial difference equations of mathematical physics. *IBM Journal of Research and Development*, 11(2):215–234.

De Vries, G., Hillen, T., Lewis, M., Müller, J., and Schönfisch, B. (2006). *A course in mathematical biology: quantitative modeling with mathematical and computational methods*. SIAM.

Del Moral, P. (2004). Feynman-Kac formulae. In *Feynman-Kac formulae*, pages 47–93. Springer.

D'Orsogna, M. R., Suchard, M. A., and Chou, T. (2003). Interplay of chemotaxis and chemokinesis mechanisms in bacterial dynamics. *Physical Review E*, 68(2):021925.

Emonet, T., Macal, C. M., North, M. J., Wickersham, C. E., and Cluzel, P. (2005). Agentcell: a digital single-cell assay for bacterial chemotaxis. *Bioinformatics*, 21(11):2714–2721.

Fama, E. F. (1995). Random walks in stock market prices. *Financial Analysts Journal*, 51(1):75–80.

Fok, P.-W., Han, Q., and Chou, T. (2015). Reconstruction of a persistent random walk from exit time distributions. *The IMA Journal of Applied Mathematics*, 80(1):1–23.

Fu, X., Kato, S., Long, J., Mattingly, H. H., He, C., Vural, D. C., Zucker, S. W., and Emonet, T. (2018). Spatial self-organization resolves conflicts between individuality and collective migration. *Nature Communications*, 9(1):1–12.

Gardiner, C. (2009). Stochastic methods: a handbook for the natural and social sciences 4th Ed.

Goldstein, S. (1951). On diffusion by discontinuous movements, and on the telegraph equation. *The Quarterly Journal of Mechanics and Applied Mathematics*, 4(2):129–156.

Grimmett, G. and Stirzaker, D. (2020). *Probability and random processes*. Oxford University Press.

Hillen, T. (2002). Hyperbolic models for chemosensitive movement. *Mathematical Models and Methods in Applied Sciences*, 12(07):1007–1034.

Hillen, T. and Painter, K. J. (2009). A user's guide to PDE models for chemotaxis. *Journal of Mathematical Biology*, 58(1):183–217.

Hoffman, J. D. and Frankel, S. (2018). *Numerical methods for engineers and scientists*. CRC Press.

Holmes, E. E. (1993). Are diffusion models too simple? A comparison with telegraph models of invasion. *The American Naturalist*, 142(5):779–795.

Holubec, A. and Stauffer, A. (1985). Efficient solution of differential equations by analytic continuation. *Journal of Physics A: Mathematical and General*, 18(12):2141.

Howell, K. B. (2019). *Ordinary differential equations: an introduction to the fundamentals*. CRC Press.

Humi, M. and Miller, W. (2012). *Second course in ordinary differential equations for scientists and engineers*. Springer Science & Business Media.

Jaynes, E. T. (2003). *Probability theory: the logic of science*. Cambridge University Press.

Kac, M. (1974). A stochastic model related to the telegrapher's equation. *The Rocky Mountain Journal of Mathematics*, 4(3):497–509.

Kaplan, S. et al. (1964). Differential equations in which the poisson process plays a role. *Bulletin of the American Mathematical Society*, 70(2):264–268.

Keller, E. F. and Segel, L. A. (1970). Initiation of slime mold aggregation viewed as an instability. *Journal of Theoretical Biology*, 26(3):399–415.

Kolesnik, A. D. (2015). The explicit probability distribution of the sum of two telegraph processes. *Stochastics and Dynamics*, 15(02):1550013.

Kolesnik, A. D. (2018). Linear combinations of the telegraph random processes driven by partial differential equations. *Stochastics and Dynamics*, 18(04):1850020.

Lax, P. D. (1973). *Hyperbolic systems of conservation laws and the mathematical theory of shock waves*. SIAM.

LeVeque, R. J. (2007). *Finite difference methods for ordinary and partial differential equations: steady-state and time-dependent problems*. SIAM.

Levy, R. A. (1967). Random walks: reality or myth. *Financial Analysts Journal*, 23(6):69–77.

Logan, J. D. (2013). *Applied mathematics*. John Wiley & Sons.

Lushi, E. and Peskin, C. S. (2013). Modeling and simulation of active suspensions containing large numbers of interacting micro-swimmers. *Computers & Structures*, 122:239–248.

Martens, K., Angelani, L., Di Leonardo, R., and Bocquet, L. (2012). Probability distributions for the run-and-tumble bacterial dynamics: an analogy to the Lorentz model. *The European Physical Journal E*, 35(9):84.

Merton, R. C. (1974). On the pricing of corporate debt: The risk structure of interest rates. *The Journal of Finance*, 29(2):449–470.

Nelsen, R. B. (2007). *An introduction to copulas*. Springer Science & Business Media.

Oosterlee, C. W. and Grzelak, L. A. (2019). *Mathematical modeling and computation in finance: with exercises and Python and MATLAB computer codes*. World Scientific.

Othmer, H. G., Dunbar, S. R., and Alt, W. (1988). Models of dispersal in biological systems. *Journal of Mathematical Biology*, 26(3):263–298.

Palais, R. S. and Palais, R. A. (2009). *Differential equations, mechanics, and computation*, volume 51. American Mathematical Soc.

Place, A. R., Bowers, H. A., Bachvaroff, T. R., Adolf, J. E., Deeds, J. R., and Sheng, J. (2012). Karlodinium veneficum—the little dinoflagellate with a big bite. *Harmful Algae*, 14:179–195.

Pollard, D. (2002). *A user's guide to measure theoretic probability*. Number 8. Cambridge University Press.

Richtmyer, R. D. and Morton, K. W. (1994). Difference methods for initial-value problems. *Malabar*.

Risken, H. (1996). Fokker-Planck equation. In *The Fokker-Planck Equation*, pages 63–95. Springer.

Sengupta, A., Kruppa, T., and Löwen, H. (2011). Chemotactic predator-prey dynamics. *Physical Review E*, 83(3):031914.

Shen, W. (2019). *Introduction To Numerical Computation, An*. World Scientific.

Sheng, J., Malkiel, E., Katz, J., Adolf, J. E., and Place, A. R. (2010). A dinoflagellate exploits toxins to immobilize prey prior to ingestion. *Proceedings of the National Academy of Sciences*, 107(5):2082–2087.

Stevens, A. and Othmer, H. G. (1997). Aggregation, blowup, and collapse: the abc's of taxis in reinforced random walks. *SIAM Journal on Applied Mathematics*, 57(4):1044–1081.

Strang, G. (2007). *Computational science and engineering*. Wellesley-Cambridge Press Cambridge.

Strang, G. (2019). *Linear algebra and learning from data*. Wellesley-Cambridge Press Cambridge.

Strang, G. and Freund, L. (1986). Introduction to applied mathematics. *Journal of Applied Mechanics*, 53(2):480.

Taktikos, J., Zaburdaev, V., and Stark, H. (2011). Modeling a self-propelled autochemotactic walker. *Physical Review E*, 84(4):041924.

Walsh, J. B. (2012). *Knowing the odds: an introduction to probability*, volume 139. American Mathematical Soc.

Wang, Z. and Hillen, T. (2008). Shock formation in a chemotaxis model. *Mathematical Methods in the Applied Sciences*, 31(1):45–70.

Yee, H., Warming, R., and Harten, A. (1985). Implicit total variation diminishing (TVD) schemes for steady-state calculations. *Journal of Computational Physics*, 57(3):327–360.

Appendix

DERIVATION AND PROOF

A.1 η as a global constant

We aim to show that η is the same constant across the domain.

Proof. At first it is clear that η is constant within each I_i. Denote the value of η in each I_i as η_i. Since x_2 is arbitrary, we must have $\eta_2 = \eta_3$. We now prove $\eta_1 = \eta_2$ and $\eta_4 = \eta_3$:

Consider the original integral conservation forms of (3.15) then sum them up over $\Omega = [x_a, x_b] \subset [0, 1]$, a subinterval of the periodic domain:

$$\frac{\partial}{\partial t} \int_{x_a}^{x_b} \Sigma dx + (s\Delta - \Sigma)\Big|_{x_a}^{x_b} = 0.$$

Now consider the steady-state: for any Ω the temporal differentiation term is 0. Let $\Omega = [x_3 - \varepsilon, x_3 + \varepsilon]$:

$$(s\Delta - \Sigma)\Big|_{x_3-\varepsilon}^{x_3+\varepsilon} = \eta_4 - \eta_3 \to 0, \quad \text{as } \varepsilon \to 0. \tag{A.1}$$

Hence $\eta_3 = \eta_4$. Similarly one can prove $\eta_1 = \eta_2$. Thus η is a constant throughout the domain. □

A.2 Proof of $\lim_{x \to x_1} |\mu\xi| = \infty$ and $\lim_{x \to x_3} \mu\xi = 0$

Lemma 1. μ near $x_i = x_1, x_3$ has the form

$$\mu = |x - x_i|^{-\nu(x_i)} G_\mu T_\mu(x), \tag{A.2}$$

where $T_\mu(x)$ is a Taylor series with constant term 1, G_μ is a non-zero constant.

Proof. We will perform the analysis for $\mu_1(x)$ near x_1 with $x < x_1$. As a reminder, $\mu_i(x)$ is defined on (x_{i-1}, x_i), $i = 1, 2, 3, 4$. For the rest of the 3 cases: μ_2 near x_1, μ_3, μ_4 near x_3 the same procedure follows. Suppose $s(x) = 1 + \sum_{j=1}^{\infty} s_j (x - x_i)^j$ near x_i, we have the following:

$$\begin{aligned}
\mu_1(x) &= \exp\left[\int_0^x \frac{2}{(s+1)(s-1)} dz\right] \\
&= \exp\left[\int_0^x \frac{2}{(2 + s_1(z-x_1) + ...)\,(s_1 + s_2(z-x_1) + ...)\,(z-x_1)} dz\right] \\
&= \exp\left[\frac{1}{s_1}\int_0^x \frac{1}{z-x_1}\left(1 - (\frac{s_1^2 + 2s_2}{2s_2})(z-x_1) + O(z-x_1)^2\right) dz\right] \\
&= \exp\left[\frac{1}{s_1}\ln|x-x_1| - \frac{1}{s_1}\ln(x_1) - \frac{1}{s_1}\int_0^x \frac{s_1^2 + 2s_2}{2s_2} + O(z-x_1) dz\right] \\
&= |x-x_1|^{-\nu(x_1)} G_\mu T_\mu(x) \qquad \text{(A.3)}
\end{aligned}$$

for some Taylor series $T_\mu(x)$ with constant term 1, and a non-zero constant G_μ. □

Lemma 2. ξ near $x_i = x_1, x_3$ can be written as

$$\xi = 2P_+(s-1) - \eta \qquad \text{(A.4)}$$

with the forms below: When $\nu(x_i) - 1 \notin \mathbb{Z}$:

$$\xi = \left(2\sum_{j=1}^{\infty} s_j (x - x_i)^{j-1}\right)\left(|x-x_i| G_{1,i}^+ T_{1,i}^+(x) + |x-x_i|^{\nu(x_i)} G_{2,i}^+ T_{2,i}^+(x)\right) - \eta. \qquad \text{(A.5)}$$

When $\nu(x_i) = 1$:

$$\begin{aligned}
\xi = \left(2\sum_{j=1}^{\infty} s_j (x - x_i)^{j-1}\right)\Big(&|x-x_i| G_{1,i}^+ T_{1,i}^+(x) + |x-x_i|^2 G_{2,i}^+ T_{2,i}^+(x) \\
&+ |x-x_i| G_{2,i}^+ \ln|x-x_i| T_{1,i}^+(x)\Big) - \eta. \qquad \text{(A.6)}
\end{aligned}$$

When $\nu(x_i) - 1 \in \mathbb{Z} - \{0\}$:

$$\begin{aligned}
\xi = \left(2\sum_{j=1}^{\infty} s_j (x - x_i)^{j-1}\right)\Big(&|x-x_i| G_{1,i}^+ T_{1,i}^+(x) + |x-x_i|^{\nu(x_i)} G_{2,i}^+ T_{2,i}^+(x) \\
&+ |x-x_i| K G_{2,i}^+ \ln|x-x_i| T_{1,i}^+(x)\Big) - \eta. \qquad \text{(A.7)}
\end{aligned}$$

As a reminder, $G^+_{2,3} = 0$ in (A.5-A.7), so that $P_\pm$ stay integrable.

Proof. From (3.34) we get $\xi = 2P_+(s-1) - \eta$, together with the Frobenius series representations of P_+ at x_i we arrive at the result. □

Theorem. $\lim_{x\to x_1} |\mu\xi| = \infty$ *and* $\lim_{x\to x_3} \mu\xi = 0$.

Proof. As a reminder, $\nu(x_i) = -\frac{1}{s'(x_i)}$, with $\nu(x_1) > 0$ and $\nu(x_3) < 0$. Using (A.3, A.5-A.7), for $\nu(x_1) - 1 \notin \mathbb{Z}$:

$$\begin{aligned}\mu\xi = \left(2\sum_{j=1}^{\infty} s_j (x-x_1)^{j-1}\right) \big(&G^+_{2,1} G_\mu T_\mu(x) T^+_{2,1}(x) \\ &+ |x-x_1|^{1-\nu(x_1)} G^+_{1,1} G_\mu T_\mu(x) T^+_{1,1}(x)\big) - \eta |x-x_1|^{-\nu(x_1)} G_\mu T_\mu(x);\end{aligned} \tag{A.8}$$

for $\nu(x_1) = 1$:

$$\begin{aligned}\mu\xi = \left(2\sum_{j=1}^{\infty} s_j (x-x_1)^{j-1}\right) \big(&|x-x_1| G^+_{2,1} G_\mu T_\mu(x) T^+_{2,1}(x) + G^+_{1,1} G_\mu T_\mu(x) T^+_{1,1}(x) \\ &+ G^+_{2,1} G_\mu \ln|x-x_1| T_\mu(x) T^+_{1,1}(x)\big) - \eta |x-x_1|^{-1} G_\mu T_\mu(x);\end{aligned} \tag{A.9}$$

and for $\nu(x_1) - 1 \in \mathbb{Z} - \{0\}$:

$$\begin{aligned}\mu\xi = \left(2\sum_{j=1}^{\infty} s_j (x-x_1)^{j-1}\right) \big(&G^+_{2,1} G_\mu T_\mu(x) T^+_{2,1}(x) + |x-x_1|^{1-\nu(x_1)} G^+_{1,1} G_\mu T_\mu(x) T^+_{1,1}(x) \\ &+ |x-x_1|^{1-\nu(x_1)} K G^+_{2,1} G_\mu \ln|x-x_1| T_\mu(x) T^+_{1,1}(x)\big) - \eta |x-x_1|^{-\nu(x_1)} G_\mu T_\mu(x).\end{aligned} \tag{A.10}$$

Near x_1, from $\nu(x_1) > 0$, we have $|x-x_i|^{-\nu(x_1)}$ dominating in (A.8-A.10) as $x \to x_1$. Therefore $\lim_{x\to x_1} |\mu\xi| = \infty$.

For $\nu(x_3)$, using $G^+_{2,3} = 0$:

$$\begin{aligned}\mu\xi = \left(2\sum_{j=1}^{\infty} s_j (x-x_3)^{j-1}\right) &\big(|x-x_3|^{1-\nu(x_3)} G^+_{1,3} G_\mu T_\mu(x) T^+_{1,3}(x)\big) \\ &- \eta |x-x_3|^{-\nu(x_3)} G_\mu T_\mu(x);\end{aligned} \tag{A.11}$$

Since $\nu(x_3) < 0$, it is immediate that $\lim_{x\to x_3} \mu\xi = 0$. □

A.3 Calculating the constants a_1-a_4 and η

We aim to show how (i)-(iv) are constructed. For convenience, first denote the constant

$$a_i = \tilde{a}_i \eta, \tag{A.12}$$

then we introduce the definition of $\mathcal{I}_i(x)$ and rewrite $\xi_i(x)$ as in Table A.1:

Table A.1: Definitions of μ, $\mathcal{I}$ and ξ in each interval.

	$\mathcal{I}_i(x)$	$\mu_i(x)$	$\xi_i(x)$
$i=1,\ x\in[0,x_1)$	$\int_0^x \frac{s\mu_1(z)}{s^2(z)-1}dz$	$\exp\left(\int_0^x \frac{2}{s^2(z)-1}dz\right)$	$\frac{\eta}{\mu_1(x)}(-2\mathcal{I}_1(x)+\tilde{a}_1)$
$i=2,\ x\in(x_1,x_2]$	$\int_x^{x_2} \frac{s\mu_2(z)}{s^2(z)-1}dz$	$\exp\left(-\int_x^{x_2} \frac{2}{s^2(z)-1}dz\right)$	$\frac{\eta}{\mu_2(x)}(2\mathcal{I}_2(x)+\tilde{a}_2)$
$i=3,\ x\in(x_2,x_3)$	$\int_{x_2}^x \frac{s\mu_3(z)}{s^2(z)-1}dz$	$\exp\left(\int_{x_2}^x \frac{2}{s^2(z)-1}dz\right)$	$\frac{\eta}{\mu_3(x)}(-2\mathcal{I}_3(x)+\tilde{a}_3)$
$i=4,\ x\in(x_3,1]$	$\int_x^1 \frac{s\mu_4(z)}{s^2(z)-1}dz$	$\exp\left(-\int_x^1 \frac{2}{s^2(z)-1}dz\right)$	$\frac{\eta}{\mu_4(x)}(2\mathcal{I}_4(x)+\tilde{a}_4)$

We note that

$$1 = \lim_{x\to 0^+}\mu_1(x) = \lim_{x\to x_2^-}\mu_2(x) = \lim_{x\to x_2^+}\mu_3(x) = \lim_{x\to 1^-}\mu_4(x), \tag{A.13}$$

and as a result

$$0 = \lim_{x\to 0^+}\mathcal{I}_1(x) = \lim_{x\to x_2^-}\mathcal{I}_2(x) = \lim_{x\to x_2^+}\mathcal{I}_3(x) = \lim_{x\to 1^-}\mathcal{I}_4(x). \tag{A.14}$$

Therefore, using (I) we get (i):

$$\lim_{x\to 0^+}\xi_1(x) = \lim_{x\to 1^-}\xi_4(x) \quad\Rightarrow\quad \tilde{a}_1 = \tilde{a}_4 \quad\Rightarrow\quad a_1 = a_4. \tag{A.15}$$

Similarly, using (II) we get (ii):

$$\lim_{x\to x_2^-}\xi_2(x) = \lim_{x\to x_2^+}\xi_3(x) \quad\Rightarrow\quad \tilde{a}_2 = \tilde{a}_3 \quad\Rightarrow\quad a_2 = a_3. \tag{A.16}$$

We then use (**III**) to get (**iii**):

$$\lim_{x\to x_3^-}\mu_3\xi_3 = 0 = \lim_{x\to x_3^-} -2\eta\mathcal{I}_3(x) + \tilde{a}_3\eta.$$

Therefore

$$\tilde{a}_3\eta = 2\mathcal{I}_3(x_3^-) \quad \Rightarrow \quad a_3 = 2\mathcal{I}_3(x_3^-) = 2\int_{x_2}^{x_3^-}\frac{s\mu_3(z)}{s^2(z)-1}dz. \tag{A.17}$$

Similarly from (**IV**) to (**iv**):

$$\tilde{a}_4\eta = -2\mathcal{I}_4(x_3^+) \quad \Rightarrow \quad a_4 = -2\mathcal{I}_4(x_3^+) = -2\int_{x_3^+}^{1}\frac{s\mu_4(z)}{s^2(z)-1}dz. \tag{A.18}$$

Within each interval I_i we can also use the formula (3.32) to compute Σ:

$$\Sigma(x) = \frac{1}{2}\left(\frac{\xi(x)+\eta}{s(x)-1} + \frac{\xi(x)-\eta}{s(x)+1}\right) = \frac{s\xi+\eta}{s^2-1}.$$

Since each ξ_i is known up to by the constant multiple of η, we use (**V**): $\int_0^1\Sigma(x) = 1$ to get (**v**):

$$\sum_{i=1}^{4}\left[\int_{I_i}\frac{s(x)\xi_i(x)+\eta}{s^2(x)-1}dx\right] = 1. \tag{A.19}$$

Specifically we can let

$$\frac{\Sigma(x)}{\eta} = \begin{cases} \frac{\frac{2s}{\mu_1(x)}\left(-\mathcal{I}_1(x)-\mathcal{I}_4(x_3^+)\right)+1}{s^2(x)-1}, & 0\le x<x_1 \\ \frac{\frac{2s}{\mu_2(x)}\left(\mathcal{I}_2(x)+\mathcal{I}_3(x_3^-)\right)+1}{s^2(x)-1}, & x_1<x\le x_2 \\ \frac{\frac{2s}{\mu_3(x)}\left(-\mathcal{I}_3(x)+\mathcal{I}_3(x_3^-)\right)+1}{s^2(x)-1}, & x_2<x<x_3 \\ \frac{\frac{2s}{\mu_4(x)}\left(\mathcal{I}_4(x)-\mathcal{I}_4(x_3^+)\right)+1}{s^2(x)-1}, & x_3<x\le 1 \end{cases} = \Sigma_0(x), \tag{A.20}$$

which no longer depends on η, to get

$$\eta = \frac{1}{\int_0^1\Sigma_0(x)dx}. \tag{A.21}$$